

Influence of CO₂ observations on the optimized CO₂ flux in an ensemble Kalman filter

JinWoong Kim¹, Hyun Mee Kim¹ and Chun-Ho Cho²

[1]{Atmospheric Predictability and Data Assimilation Laboratory

Department of Atmospheric Sciences, Yonsei University, Seoul, Republic of Korea}

[2]{National Institute of Meteorological Research, Jeju, Republic of Korea}

Correspondence to: Hyun Mee Kim (khm@yonsei.ac.kr)

Abstract

In this study, the effect of CO₂ observations on an analysis of surface CO₂ flux were calculated using an influence matrix in the CarbonTracker, which is an inverse modeling system for estimating surface CO₂ flux based on an ensemble Kalman filter. The influence matrix represents a sensitivity of the analysis to observations. The experimental period was from January 2000 to December 2009. The diagonal element of the influence matrix (i.e., analysis sensitivity) is globally 4.8% on average, which implies that the analysis extracts 4.8% of the information from the observations and 95.2% from the background each assimilation cycle. Because the surface CO₂ flux in each week is optimized by five weeks of observations, the cumulative impact over five weeks is 19.1%, much greater than 4.8%. The analysis sensitivity is inversely proportional to the number of observations used in the assimilation, which is distinctly apparent in continuous observation categories with a sufficient number of observations. The time series of the globally averaged analysis sensitivities shows seasonal variations, with greater sensitivities in summer and lower sensitivities in winter, which is attributed to the surface CO₂ flux uncertainty. The time-averaged analysis sensitivities in the Northern Hemisphere are greater than those in the Tropics and the Southern Hemisphere. The trace of the influence matrix (i.e., information content) is a measure of the total information extracted from the observations. The information content indicates an imbalance between the observation coverage in North

1 America and that in other regions. Approximately half of the total observational information
2 is provided by continuous observations, mainly from North America, which indicates that
3 continuous observations are the most informative and that comprehensive coverage of
4 additional observations in other regions is necessary to estimate the surface CO₂ flux in these
5 areas as accurately as in North America.

6 **1 Introduction**

7 Atmospheric CO₂ observations can be used to quantitatively estimate the sources and sinks of
8 surface carbon fluxes. Thus, atmospheric CO₂ inversion studies using atmospheric CO₂
9 observations have been conducted (Gurney et al., 2002; Ciais et al., 2010; Peylin et al., 2013).
10 Various studies applying state-of-the-art data assimilation methods have been carried out to
11 estimate the surface carbon cycle at global and regional scales. The methods employed for
12 the atmospheric CO₂ inversion studies include variational data assimilation methods
13 (Chevallier et al., 2005, 2009a, 2009b; Baker et al., 2006, 2010; Basu et al., 2013), ensemble
14 Kalman filter (EnKF) (Peters et al., 2005, 2007, 2010; Feng et al., 2009; Miyazaki et al.,
15 2011; Kang et al., 2011, 2012; Chatterjee et al., 2012; Kim et al., 2012, 2014), and maximum
16 likelihood ensemble filter (Zupanski et al., 2007; Lokupitiya et al., 2008). These studies have
17 applied the data assimilation method used in numerical weather prediction (NWP) to estimate
18 surface CO₂ fluxes.

19 Recent studies on atmospheric CO₂ inversion have focused on analyzing the difference
20 between prior and optimized surface CO₂ fluxes obtained by using new inversion methods or
21 observations (Chevallier et al., 2009a; Basu et al., 2013), as well as the carbon cycle based on
22 optimized surface CO₂ fluxes. By contrast, the impact of various atmospheric CO₂
23 observations on the estimation of surface CO₂ fluxes has rarely been studied. One method
24 employed to evaluate the impact of observations on atmospheric CO₂ inversion is the
25 calculation of the uncertainty reduction (Peters et al., 2005; Meirink et al., 2008; Chevallier et
26 al., 2009b; Feng et al., 2009), which is a ratio between the variances of the prior and posterior
27 state vectors. A large uncertainty reduction implies that observations have a large impact on
28 the estimation of surface CO₂ fluxes. However, the uncertainty reduction cannot measure the
29 impact of individual observations on the estimated (i.e., analyzed) surface CO₂ fluxes.
30 Another method for assessing the impact of observations is to calculate the information
31 content, which is the amount of information obtained from observations (Rodgers, 2000).

1 Engelen and Stephen (2004) calculated the information content of infrared satellite sounding
2 observations on atmospheric CO₂ concentrations. To estimate the impact of simulated CO₂
3 observations on surface flux analysis, Zupanski et al. (2007) calculated the information
4 content using the information matrix in the ensemble subspace. However, similar to the
5 uncertainty reduction, these methods calculate the impact of all observations, rather than
6 calculating the impact of individual observations on surface CO₂ flux analysis.

7 Data assimilation algorithms are fundamentally based on a linear statistical assumption
8 (Talagrand, 1997). Both sequential and variational algorithms combine background and
9 observation information to estimate parameters based on the linear assumption. According to
10 the linear assumption, the influence matrix that measures the impact of individual
11 observations on estimated parameters can be calculated in the observation space. Cardinali et
12 al. (2004) suggested a method for calculating the influence matrix within the general data
13 assimilation framework and applied the method to a forecast model of the European Centre
14 for Medium Weather Forecasts (ECMWF). The diagonal elements of the influence matrix are
15 the analysis sensitivities (i.e., self-sensitivity), which are proportional to the spread of the
16 analysis and are inversely proportional to the predetermined observation error. The trace of
17 the diagonal elements of the influence matrix reflects the information content, which is the
18 amount of information extracted from observations. The influence matrix provides objective
19 diagnostics regarding the impact of observations on the analysis and hence the performance
20 of the data assimilation system because inaccurate observations can be identified by
21 analyzing the observation impact (Cardinali et al., 2004). Liu et al. (2009) suggested a
22 method for calculating self-sensitivity and cross-sensitivity (i.e., off-diagonal elements of the
23 influence matrix) within the EnKF framework and diagnosed the relative importance of
24 individual observations within an observation system using the idealized Lorenz-40 model
25 and the simplified hydrostatic model.

26 Although Cardinali et al. (2004) and Liu et al. (2009) suggested methods for calculating the
27 impact of individual observations on an analysis, their studies focused on NWP. Therefore,
28 the impact of individual observations on surface CO₂ flux analysis has not been diagnosed in
29 a study on atmospheric CO₂ inversion using the state-of-the-art data assimilation method.
30 Because the analysis is more important than the forecast in atmospheric CO₂ inversion, the

1 methods suggested by Cardinali et al. (2004) and Liu et al. (2009) can be applied to diagnose
2 the impact of observations on the CO₂ flux analysis.

3 CarbonTracker is a system developed by the National Oceanic and Atmospheric
4 Administration (NOAA), which optimizes the surface CO₂ flux by assimilating mole fraction
5 observations (i.e., concentration) of surface CO₂ (Peters et al., 2005). CarbonTracker has
6 been applied in studies on atmospheric CO₂ inversion in North America (Peters et al., 2010),
7 Europe (Peters et al., 2010), and Asia (Kim et al. 2014). To develop CarbonTracker for use in
8 Asia, Kim et al. (2012) performed an experiment employing CarbonTracker in this region
9 and demonstrated that CarbonTracker produces optimized surface CO₂ fluxes for Asia. Kim
10 et al. (2014) showed that the estimates of the surface CO₂ flux are more consistent with
11 observed CO₂ concentrations in Asia when using the nesting domain of the transport model
12 on Asia in CarbonTracker. Zhang et al. (2014) conducted a study on the assimilation of
13 aircraft CO₂ observations from the Comprehensive Observation Network for TRace gases by
14 AirLiner (CONTRAIL) (Machida et al., 2008) in Asia using CarbonTracker.

15 In this study, an influence matrix is calculated in CarbonTracker to evaluate the impact of
16 mole fraction observations of CO₂ on the analyzed surface CO₂ fluxes. The relative
17 importance of each observation site and each observation site category is evaluated by
18 analyzing the self-sensitivity and information content, and the characteristics of the self-
19 sensitivity and information content are subsequently investigated. Section 2 presents the
20 experimental framework, which includes CarbonTracker, EnKF, observations, the
21 methodology for calculating the influence matrix, and the experimental framework. Section 3
22 presents the results, and Section 4 provides a summary and conclusion.

23 **2 Methodology**

24 **2.1 CarbonTracker**

25 CarbonTracker is an atmospheric CO₂ inversion system that estimates the surface CO₂ flux
26 consistent with CO₂ observations. In CarbonTracker, the optimized flux with a 1°×1°
27 horizontal resolution is calculated by

$$28 \quad F(x, y, t) = \lambda_r \cdot F_{bio}(x, y, t) + \lambda_r \cdot F_{ocn}(x, y, t) + F_{ff}(x, y, t) + F_{fire}(x, y, t), \quad (1)$$

1 where $F_{bio}(x, y, t)$ is the prescribed prior biosphere flux from the Carnegie Ames Stanford
2 Approach Global Fire Emissions Database (CASA GFED) version 3.1 (van der Werf et al.,
3 2010); $F_{ocn}(x, y, t)$ is the prescribed prior ocean flux based on Jacobson et al. (2007);
4 $F_{ff}(x, y, t)$ is the prescribed prior fossil fuel flux determined using the Carbon Dioxide
5 Information and Analysis Center (CDIAC) and the Emission Database for Global
6 Atmospheric Research (EDGAR) inventories; $F_{fire}(x, y, t)$ is the prescribed prior fire flux
7 derived from CASA GFED version 3.1 (van der Werf et al., 2010); and λ_r is the scaling
8 factor to be optimized in the data assimilation process, corresponding to 156 ecoregions
9 around the globe. CarbonTracker adopts a smoother window to reflect the transport speed of
10 CO_2 , which is based on the temporal relationship between the surface CO_2 flux and
11 atmospheric CO_2 observations, as found in Bruhwiler et al. (2005) (Peters et al., 2005). For
12 this reason, the scaling factor is optimized for five weeks of lag, which implies that the
13 observations made in the most recent week affect the optimized surface CO_2 flux in the
14 preceding four weeks. The optimization of the scaling factor during the data assimilation
15 process is presented in Fig. 1. In each assimilation cycle, five weeks of analysis scaling
16 factors are estimated by observations from the most recent week. After the fifth cycle, the
17 scaling factor estimated by these five weeks of observations is saved as the optimized scaling
18 factor and used to calculate the optimized surface CO_2 flux in Eq. (1). During this process, a
19 new mean background scaling factor for the next week is calculated by the estimated mean
20 scaling factors of the previous two weeks using a simple dynamic model, as follows:

$$21 \quad \lambda_t^b = \frac{(\lambda_{t-2}^a + \lambda_{t-1}^a + \lambda^p)}{3}, \quad (2)$$

22 where λ_t^b is a prior mean scaling factor for the new analysis week; λ_{t-2}^a and λ_{t-1}^a are
23 posterior mean scaling factors estimated two weeks and one week previous, respectively; and
24 λ^p is a prior value fixed as 1. Thus, the information from the previous observations is
25 included in λ_t^b .

26 The TM5 model (Krol et al., 2005) is used as a transport model that calculates model CO_2
27 concentrations corresponding to the observed CO_2 concentrations. The TM5 model uses the
28 surface CO_2 fluxes calculated from Eq. (1) and the ECMWF meteorological field to calculate

1 model CO₂ concentrations and is used as the observation operator, which will be explained in
 2 Section 2.2.

3 **2.2 Ensemble Kalman Filter**

4 The EnKF data assimilation method used in CarbonTracker is the ensemble square root filter
 5 (EnSRF) suggested by Whitaker and Hamill (2002). The analysis equation for data
 6 assimilation is expressed as

$$7 \quad \mathbf{x}^a = \mathbf{K}\mathbf{y}^o + (\mathbf{I}_n - \mathbf{K}\mathbf{H})\mathbf{x}^b, \quad (3)$$

8 where \mathbf{x}^a is the n -dimensional analysis (posterior) state vector; \mathbf{y}^o is the p -dimensional
 9 observation vector; \mathbf{K} is the $n \times p$ dimensional Kalman gain; \mathbf{I}_n is the identical matrix; \mathbf{H} is
 10 the linearized observation operator, which transforms the information in the model space to
 11 the information in the observation space; and \mathbf{x}^b is the background state vector. In EnSRF,
 12 the ensemble mean and perturbed state vectors are updated independently using the following
 13 equations:

$$14 \quad \mathbf{x}^a = \mathbf{x}^b + \mathbf{K}(\mathbf{y}^o - \mathbf{H}\mathbf{x}^b), \quad (4)$$

$$15 \quad \mathbf{x}'_i{}^a = \mathbf{x}'_i{}^b - \tilde{\mathbf{k}}\mathbf{H}\mathbf{x}'_i{}^b, \quad (5)$$

16 where \mathbf{x}^a and \mathbf{x}^b are mean state vectors of the analysis and background, respectively, and
 17 $\mathbf{x}'_i{}^a$ and $\mathbf{x}'_i{}^b$ are perturbation state vectors of the analysis and background, respectively.
 18 Many inflation techniques (e.g., Wang and Bishop, 2003; Bowler et al., 2008; Whitaker et al.,
 19 2008; Li et al., 2009; Anderson, 2009; Miyoshi, 2011; Kang et al., 2012) have been used to
 20 maintain proper ensemble spread and to improve the performance of EnKF data assimilation.
 21 Although the EnSRF in CarbonTracker does not use the inflation method, Kim et al. (2012)
 22 demonstrated that the ensemble spread measured by rank histograms is maintained properly.
 23 In CarbonTracker, the state vector corresponds to the scaling factor, as described in Section
 24 2.1. \mathbf{K} and the reduced Kalman gain, $\tilde{\mathbf{k}}$, are defined as

$$25 \quad \mathbf{K} = (\mathbf{P}^b\mathbf{H}^T)(\mathbf{H}\mathbf{P}^b\mathbf{H}^T + \mathbf{R})^{-1}, \quad (6)$$

$$26 \quad \tilde{\mathbf{k}} = \mathbf{K} \cdot \alpha, \quad (7)$$

1 where \mathbf{P}^b is the background error covariance; \mathbf{R} is the observation error covariance, which is
 2 predefined at each observation site; and α is a scalar value that varies whenever each
 3 observation is used in the analysis process and is calculated as

$$4 \quad \alpha = \left(1 + \sqrt{\frac{\mathbf{R}}{\mathbf{H}\mathbf{P}^b\mathbf{H}^T + \mathbf{R}}} \right)^{-1}, \quad (8)$$

5 $\mathbf{P}^b\mathbf{H}^T$ and $\mathbf{H}\mathbf{P}^b\mathbf{H}^T$ in Eqs. (6) and (8) can be calculated as

$$6 \quad \mathbf{P}\mathbf{H}^T \approx \frac{1}{m-1} (\mathbf{x}'_1, \mathbf{x}'_2, \dots, \mathbf{x}'_m) \cdot (\mathbf{H}\mathbf{x}'_1, \mathbf{H}\mathbf{x}'_2, \dots, \mathbf{H}\mathbf{x}'_m)^T, \quad (9)$$

$$7 \quad \mathbf{H}\mathbf{P}\mathbf{H}^T \approx \frac{1}{m-1} (\mathbf{H}\mathbf{x}'_1, \mathbf{H}\mathbf{x}'_2, \dots, \mathbf{H}\mathbf{x}'_m) \cdot (\mathbf{H}\mathbf{x}'_1, \mathbf{H}\mathbf{x}'_2, \dots, \mathbf{H}\mathbf{x}'_m)^T, \quad (10)$$

8 where m is the number of ensembles.

9 To reduce the sampling error and filter divergence due to the underestimation of background
 10 error covariance in EnSRF, the covariance localization method is used (Houtekamer and
 11 Mitchell, 2001). Because the physical distance between the scaling factors cannot be defined
 12 in CarbonTracker, correlations between the ensemble of the scaling factor and the ensemble
 13 of the model CO₂ concentration are calculated, and a statistical significance test is performed
 14 on the correlations. Then, the Kalman gain which has an insignificant statistical value is set to
 15 zero. This type of localization is applied to all observation sites except for Marine Boundary
 16 Layer (MBL) sites, because the observations at MBL sites are considered to include
 17 information on large footprints of flux signals (Peters et al., 2007).

18 **2.3 Influence matrix**

19 The influence matrix for EnKF is calculated as in Liu et al. (2009). The projection of Eq. (3)
 20 onto the observation space becomes

$$21 \quad \mathbf{H}\mathbf{x}^a = \mathbf{y}^a = \mathbf{H}\mathbf{K}\mathbf{y}^o + (\mathbf{I}_p - \mathbf{H}\mathbf{K})\mathbf{y}^b, \quad (11)$$

22 where \mathbf{y}^a is the analysis value in the observation space and the projection of the state vector
 23 \mathbf{x}^a on the observation space. The influence matrix \mathbf{S}^o , representing the sensitivity of the

1 analysis state vector \mathbf{y}^a to the observation vector \mathbf{y}^o (i.e., analysis sensitivity to observation)
 2 in the observation space, is calculated as follows:

$$3 \quad \mathbf{S}^o = \frac{\partial \mathbf{y}^a}{\partial \mathbf{y}^o} = \mathbf{K}^T \mathbf{H}^T = \mathbf{R}^{-1} \mathbf{H} \mathbf{P}^a \mathbf{H}^T, \quad (12)$$

4 where \mathbf{S}^o is proportional to the analysis error covariance and is inversely proportional to the
 5 observation error covariance. By contrast, the analysis sensitivity to background is

$$6 \quad \mathbf{S}^b = \frac{\partial \mathbf{y}^a}{\partial (\mathbf{H} \mathbf{x}^b)} = \mathbf{I}_p - \mathbf{K}^T \mathbf{H}^T = \mathbf{I}_p - \mathbf{S}^o, \quad (13)$$

7 where \mathbf{y}^b is the projection of the background on the observation space, and \mathbf{I}_p is an identity
 8 matrix with the size of the number of observations. Consequently, the sum of the analysis
 9 sensitivity to observation in Eq. (12) and the analysis sensitivity to background in Eq. (13) is
 10 one.

11 Substituting Eq. (10) into Eq. (12) becomes

$$12 \quad \mathbf{S}^o = \mathbf{R}^{-1} \mathbf{H} \mathbf{P}^a \mathbf{H}^T = \frac{1}{m-1} \mathbf{R}^{-1} (\mathbf{H} \mathbf{X}^a) (\mathbf{H} \mathbf{X}^a)^T, \quad (14)$$

13 where $\mathbf{H} \mathbf{X}^a$ is the analysis ensemble perturbation matrix in the observation space, and the i^{th}
 14 column of $\mathbf{H} \mathbf{X}^a$ is calculated as

$$15 \quad \mathbf{H} \mathbf{X}_i^a \cong h(\mathbf{x}_i^a) - \frac{1}{m} \sum_{i=1}^m h(\mathbf{x}_i^a), \quad (15)$$

16 where \mathbf{x}_i^a is the i^{th} analysis ensemble member; m is the number of ensembles (i.e., 150); and
 17 $h(\cdot)$ is the linear or nonlinear observation operator. More specifically, if the observation
 18 errors are not correlated, the diagonal elements of the influence matrix (i.e., self-sensitivity)
 19 are calculated as

$$20 \quad \mathbf{S}_{jj}^o = \frac{\partial \mathbf{y}_j^a}{\partial \mathbf{y}_j^o} = \left(\frac{1}{m-1} \right) \frac{1}{\sigma_j^2} \sum_{i=1}^m (\mathbf{H} \mathbf{X}_i^a)_j \times (\mathbf{H} \mathbf{X}_i^a)_j, \quad (16)$$

21 where σ_j^2 is the error variance of the j^{th} observation. The cross-sensitivity is the off-diagonal
 22 elements of the influence matrix. The influence matrix is calculated for the most recent week

1 of each cycle because the background at the most recent week of each cycle is updated once
 2 by observations.

3 The cumulative impact of the influence matrix for the five weeks of lag can be calculated
 4 because the background in the lagged window already includes the effect from previous
 5 observations. For example, Fig. 2 shows that $\mathbf{S}^b(5)$ is affected by $\mathbf{S}^o(1)$, $\mathbf{S}^o(2)$, $\mathbf{S}^o(3)$, and
 6 $\mathbf{S}^o(4)$, where the number inside of parenthesis represent the week of the five-week
 7 assimilation lag. If $\mathbf{S}^o(\bullet)$ has a value between 0 and 1, $\mathbf{S}^b(1)$, the analysis sensitivity to
 8 background at the first week, represents an information from previous analysis cycle and is
 9 calculated as

$$10 \quad \mathbf{S}^b(1) = (1 - \mathbf{S}^o(1))(1 - \mathbf{S}^o(2))(1 - \mathbf{S}^o(3))(1 - \mathbf{S}^o(4))(1 - \mathbf{S}^o(5)), \quad (17)$$

11 Using Eq. (13), the cumulative impact of the influence matrix is

$$12 \quad \mathbf{S}_{\text{cum}}^o = 1 - \mathbf{S}^b(1) = 1 - (1 - \mathbf{S}^o(1))(1 - \mathbf{S}^o(2))(1 - \mathbf{S}^o(3))(1 - \mathbf{S}^o(4))(1 - \mathbf{S}^o(5)), \quad (18)$$

13 where $\mathbf{S}_{\text{cum}}^o$ is the cumulative impact of observations during the lagged window. The
 14 cumulative impact was defined within the five-week assimilation lag and calculated when
 15 $\mathbf{S}^o(5)$ exists.

16 The information content (i.e., degrees of freedom for signal), which is a measure of the
 17 information extracted from the observations, is calculated by the trace of the influence matrix.
 18 As suggested by Cardinali et al. (2004), the globally averaged influence of the observations
 19 can be calculated by averaging the global self-sensitivities as

$$20 \quad GAI = \frac{\text{tr}(\mathbf{S}^o)}{p}, \quad (19)$$

21 where p is the total number of observations used in each assimilation cycle. The partial
 22 influence of a subset of observations is calculated as

$$23 \quad PAI = \frac{\sum_{i \in I} S_{ii}^o}{p_I}, \quad (20)$$

1 where p_I represents the number of observations in subset I , which can either be set as
2 specific observation types or as specific vertical and horizontal domains.

3 **2.4 Observations**

4 The observations used in this study are surface CO₂ mole fraction data observed at sites
5 distributed around the globe (Table 1 and Fig. 3). As in Peters et al. (2007), the surface CO₂
6 mole fraction data used in this study includes surface air samples collected around the globe
7 and from tall towers. These data were observed by NOAA, the Commonwealth Scientific and
8 Industrial Research Organization (CSIRO), Environment Canada (EC), the National Center
9 for Atmospheric Research (NCAR), and Lawrence Berkeley National Laboratory (LBNL)
10 (Masarie et al., 2011). Observations from three additional sites made by the Japan
11 Meteorological Agency (JMA) are also used in this study. The site categories and model-data
12 mismatch values (i.e., observation error) are shown in Table 2. The model-data mismatch is
13 determined as the innovation χ^2 in Eq. (21) becomes one at each observation site (Peters et al.,
14 2007).

$$15 \quad \chi^2 = \frac{(y^o - \mathbf{H}\mathbf{x}^b)^2}{\mathbf{H}\mathbf{P}^b\mathbf{H}^T + \mathbf{R}}, \quad (21)$$

16 The innovation χ^2 statistics for each observation site in Asia during the experimental period
17 are presented in Table 3. The model-data mismatch for the TAP site (Tae-ahn peninsula,
18 South Korea; 36.73°N, 126.13°E, 20 m) was changed from the value of 7.5 ppm used in
19 previous studies to 5 ppm because the innovation χ^2 value obtained using 5 ppm was closer to
20 one. However, TAP was still included in the Difficult category in the statistical analysis in
21 Section 3. The model-data mismatches of the three JMA sites were set to 3 ppm, as in Zhang
22 et al. (2014).

23 **2.5 Experimental framework**

24 The surface carbon flux analysis system used in this study is based on the CarbonTracker
25 2010 release (CT2010). However, the system employed in this study is different from
26 CT2010 in two aspects: first, the nesting domain of the TM5 model, with 1°×1° horizontal
27 resolution, is centered in Asia rather than in North America, which enables a more detailed

1 analysis of the surface CO₂ fluxes over Asia, as shown in Kim et al. (2014); second, as
2 mentioned in Section 2.4, three new JMA observation sites are added in this system, which
3 also enhances the analysis of surface CO₂ fluxes over Asia. The global horizontal resolution
4 is 3°×2°, as in CT2010. The experimental period is from 1 January 2000 to 31 Dec 2009. The
5 number of ensembles is 150, and the scaling factor includes five weeks of lag, as in Peters et
6 al. (2007, 2010) and Kim et al. (2012, 2014).

7 **3 Results**

8 **3.1 Self-sensitivity**

9 **3.1.1 Average self-sensitivity**

10 Cardinali et al. (2004) demonstrated that the self-sensitivity is theoretically between 0 and 1
11 if observations are not correlated. In 4D-VAR, Cardinali et al. (2004) denoted that analysis
12 error covariance based on the Hessian representation with truncated eigenvector expansion
13 can introduce the self-sensitivities greater than 1 for only a small percentage of the cases. In
14 contrast, the self-sensitivity in EnKF theoretically has a value lesser than 1 (Liu et al. 2009).
15 Nevertheless, the self-sensitivity in this study shows a value greater than one because the
16 sparse observations cause insufficient reduction of the background and observation operator
17 used has nonlinearity in calculating the transport of CO₂ concentrations. In this study, 13
18 observations from the total of 76,801 observations used for data assimilation present a value
19 greater than one. This is only 0.02% of the total number of observations, which implies that
20 the calculated self-sensitivity is generally valid.

21 Because the spatial coverage and number of observations varies during the experimental
22 period, the average self-sensitivity throughout the experimental period was analyzed to
23 evaluate the overall characteristics of the self-sensitivity at each observation site. As in
24 previous studies (e.g., Peters et al., 2007, 2010; Kim et al., 2014), the results for the year
25 2000 were excluded from the data analysis because 2000 is considered as the spin-up period.

26 Figure 4 shows the average self-sensitivities at each observation site during the experimental
27 period. Different sizes of circles are used in some locations to distinguish sites at the same
28 location or at geographically close locations. In the globe, negative correlations between the
29 spatial density of the observation sites and the self-sensitivities are not as apparent as those

1 reported by Cardinali et al. (2004) and Liu et al. (2009). Negative correlations between the
2 spatial density of the observation sites and the self-sensitivities are apparent in the Northern
3 Hemisphere (NH). In particular, some observation sites in Asia show high sensitivities and a
4 low spatial density of observation sites. The observation sites located in deserts, remote
5 oceans, and high altitude regions generally exhibit low sensitivities.

6 The average self-sensitivities of each observation site category over the globe, in the NH,
7 Tropics, and Southern Hemisphere (SH) are shown in Fig. 5. The average global self-
8 sensitivity is 4.8% (Fig. 5a), which implies that the analysis extracts 4.8% of its information
9 from the observations and 95.2% from the background each assimilation cycle. Although the
10 average self-sensitivity seems low, the background contains the observation information
11 included in the previous analysis cycle, as reported in Cardinali et al. (2004). Moreover, the
12 surface CO₂ fluxes in CarbonTracker are optimized by five weeks of observations during the
13 assimilation process. Therefore, the cumulative impact over five weeks is 19.1% much
14 greater than 4.8%, which only represents the most recent week of each cycle. Although the
15 cumulative impact shows a higher value, the non-cumulative impact measured in the most
16 recent week of each cycle is used to discuss the impact of observations because the non-
17 cumulative impact has been generally used as the observation impact.

18 In the globe, the Mixed site category shows the highest average self-sensitivity, and the
19 Difficult site category shows the lowest average self-sensitivity (Fig. 5a), which is related to
20 the model-data mismatch values shown in Table 1. The model-data mismatch for the Mixed
21 site category is relatively low, while that of the Difficult site category is high. Although the
22 MBL site category has the lowest model data mismatch, the MBL site category does not
23 show the highest average self-sensitivity due to the small spread of the analysis CO₂
24 concentrations at MBL sites. As shown in Eq. (16), the model-data mismatch and the spread
25 of the analysis CO₂ concentrations are two factors determining the self-sensitivity. Because
26 MBL sites are located far from strong source and sink regions of CO₂, the spread of the
27 analysis CO₂ concentrations at these sites is small. The average self-sensitivity in the NH is
28 5.3%, which is the highest of all global regions (Fig. 5b). Similar to the global results, the
29 average self-sensitivity is highest for the Mixed site category, while that for the Difficult site
30 category is lowest. The average self-sensitivity in the Tropics is 3.6% (Fig. 5c); the Mixed
31 site category shows the highest values, but they are not significantly higher than those of

1 other categories. In the Tropics, there is no Continuous site category. In the SH, the average
2 self-sensitivity is 3.0%, which is the lowest among the global regions (Fig. 5d); the MBL site
3 category shows the highest values, and there is no Continuous site category.

4 **3.1.2 Time series of self-sensitivity**

5 Figure 6 shows the time series of the average self-sensitivity and number of observations
6 around the globe and in each region. Globally, two apparent characteristics can be identified
7 in the time series (Fig. 6a): first, the average self-sensitivity decreases as the number of
8 observations increases, showing an inversely proportional relationship; second, there is
9 seasonal variability in the average self-sensitivity, showing high values in summer and low
10 values in winter. In the NH, the above two features are more apparent than in other regions
11 (Fig. 6b). Because most of the observation sites are located in the NH, characteristics of the
12 average global self-sensitivity are mostly determined by those in the NH. As the number of
13 observations in the Tropics increases in the late 2000s, a slight inversely proportional
14 relationship between the average self-sensitivity and the number of observations appears in
15 the Tropics (Fig. 6c). However, the average self-sensitivity in the Tropics does not show
16 distinct seasonal variability. In the SH, an inverse relationship between the average self-
17 sensitivity and the number of observations is not clearly shown (Fig. 6d), which is due to the
18 insufficient increase of the number of observations assimilated in the SH compared with the
19 other regions. However, the seasonal variability of the average self-sensitivity appears clearly
20 in the SH. Therefore the inverse relationship is distinctly shown when the increase of the
21 number of observations is enough to cause the decrease of the average self-sensitivity.

22 Figure 7 shows the average self-sensitivity for each observation site category. Although the
23 MBL site category has the second largest number of observations, the average self-sensitivity
24 shows little variation with respect to time (Fig. 7a). Similarly, the average self-sensitivity for
25 the Continental site category does not vary with respect to time (Fig. 7b). The average self-
26 sensitivity of the Mixed site category shows distinct seasonal variation (Fig. 7c). The
27 Continuous site category displays distinct seasonal variability in the average self-sensitivity
28 and an inversely proportional relationship between the average self-sensitivity and the
29 number of observations (Fig. 7d). Because Continuous sites are mostly located in North
30 America with relatively large numbers (Fig. 3), the impact of a single observation decreases

1 as the number of observations increases. Therefore, the inversely proportional relationships
2 between the average self-sensitivity and the number of observations around the globe (Fig.
3 6a) and in the NH (Fig. 6b) are mainly attributed to the Continuous site category. The
4 Difficult site category shows a slight inverse relationship between the average self-sensitivity
5 and the number of observations (Fig. 7e).

6 **3.1.3 Effect of the ensemble spread of the model surface CO₂ flux on the** 7 **average self-sensitivity**

8 Despite the inversely proportional relationship between the self-sensitivity and the number of
9 observations in the NH time series (Fig. 6a), the average self-sensitivity in the NH is higher
10 than in the other regions (Fig. 5). In addition, the average self-sensitivities in the NH and SH
11 are greater in summer than in winter (Fig. 6). The above two characteristics imply that
12 another factor in addition to the number of observations affects the self-sensitivity. As briefly
13 mentioned in Section 3.2.1, another factor that affects the self-sensitivity is the spread of the
14 analysis CO₂ concentrations. Therefore, the average standard deviations of surface CO₂
15 fluxes are evaluated in Fig. 8 to investigate the influence of the surface CO₂ flux uncertainties
16 on the seasonal and regional characteristics of the self-sensitivities. The ensemble spread of
17 the background surface CO₂ fluxes reflects the uncertainties, which are projected onto the
18 ensemble spread of the background and analysis CO₂ concentrations (i.e., \mathbf{HX}^a in Eq. (16))
19 by the transport model. The uncertainties of the background surface CO₂ fluxes over the
20 terrestrial portion of the NH are high in summer months (i.e., June, July, and August: JJA)
21 (Fig. 8a) compared with those in winter months (i.e., December, January, and February: DJF)
22 (Fig. 8b). Due to the high surface CO₂ flux uncertainties in North America (Fig. 8a), the self-
23 sensitivities in North America are not lower than those in the other regions (Fig. 4),
24 regardless of the large number of observations in this region. By contrast, despite the high
25 uncertainties of the surface CO₂ fluxes in the Eurasian Boreal region, the self-sensitivities in
26 this region cannot be evaluated owing to the absence of observations. Instead, the self-
27 sensitivities of the observation sites near the Eurasian Boreal region show high values (Fig. 4).
28 The uncertainties of the optimized biosphere and ocean fluxes by one week of observations,
29 shown in Figs. 8c and d, are reduced compared with those of the background fluxes, shown in
30 Figs. 8a and b. The magnitude of the reduction of the surface CO₂ flux uncertainties in North

1 America is relatively greater than in other regions, which is consistent with the greater self-
2 sensitivities found in North America. By contrast, when using five weeks of observations, the
3 magnitude of the reduction of the surface CO₂ flux uncertainties is greater in Asia than in
4 North America (Figs. 8e and f).

5 Therefore, the surface CO₂ flux uncertainty is one of the components to determine the
6 magnitude and seasonal variation of the self-sensitivities.

7 **3.2 Information content**

8 **3.2.1 Average information content**

9 Figure 9 shows the average information content at each observation site during the
10 experimental period. This value was calculated by averaging the ratio of information contents
11 for each cycle at each site during the experimental period. Note that this average value is not
12 the amount of information content extracted from observations but rather the relative ratio of
13 each site's information content, normalized by the total influence of all observations. Because
14 the magnitude of the information content at one observation site is proportional to the self-
15 sensitivity and the number of observations, the observation sites with a high average self-
16 sensitivity or a large number of observations show high information content. The number of
17 observations at one station depends on the temporal resolution, missing rate, and total period
18 of observations. Therefore, the observation sites located in North America and Asia generally
19 show high average information content.

20 To investigate the distribution of the information content in each region, histograms of the
21 average information content around the globe and in the NH, Tropics, and SH were generated
22 (Fig. 10). The average information content was 80.2% in the NH, 13.3% in the Tropics, and
23 6.5% in the SH, which implies that the observations in the NH are the most informative. This
24 is due to the large number of observations and high self-sensitivities in the NH. Around the
25 globe, the most informative observation site category is the Continuous category (Fig. 10a).
26 The MBL, Continental, and Mixed site categories show a similar magnitude of information
27 content, but the Difficult site category shows the lowest information content. As in the globe,
28 the Continuous site category is the most informative in the NH (Fig. 10b). In the current
29 CarbonTracker system, the observation sites of the Continuous site category are mainly

1 located in North America, except for the three JMA sites, which are located in Asia.
2 Therefore, most of the information extracted from the Continuous site category is used to
3 constrain the surface CO₂ fluxes of North America. In the Tropics, the MBL and Mixed site
4 categories provide the most information (Fig. 10c). In the SH, the MBL site category
5 provides the most information, but information extracted from the Continental, Mixed, and
6 Difficult site categories is rare (Fig. 10d). In addition, the information from the Continuous
7 site category is zero because there is no Continuous data in the SH.

8 **3.2.2 Time series of information content**

9 Figure 11 shows the time series of the weekly averaged information content for each site
10 category in each region. In the globe, the proportion of the information content of the
11 Continuous site category increases steadily over time (Fig. 11a), which is associated with the
12 steady increase in the number of observations of the Continuous site category over time. In
13 the NH, the increase of the proportion of the information content and the number of
14 observations of the Continuous site category is more readily apparent (Fig. 11b). In the
15 Tropics, the MBL and Mixed site categories provide the most information, while the Difficult
16 site category provides limited information from 2004 onward (Fig. 11c) because, after this
17 date, observations from only one Difficult observation site (Bukit Kotobang (BKT),
18 Indonesia: 0.2 °S, 100.32 °E, 864 m) are used in the data assimilation. In the SH, most
19 information is extracted from observations made in the MBL site category (Fig. 11d).
20 Because the number of observations in the SH is much lower than in the other regions, the
21 information content extracted from the observations made in this region is also lower. The
22 information content in summer is greater than in winter in the SH owing to the seasonal
23 variability in self-sensitivity.

24 To investigate the regional distribution of the information content in the NH, the time series
25 of the information contents in Asia, North America, and Europe are shown in Fig. 12. The
26 information content in North America is greater than that in the other regions because the
27 self-sensitivities are high and the number of observations increases with time in North
28 America. However, the rate of increase in the information content is lower than that of the
29 number of observations because self-sensitivity decreases as the number of observations
30 increases in North America.

3.2.3 Relationship between the information content and the optimized flux

Because CarbonTracker is a system that optimizes the surface CO₂ flux using measurements of surface CO₂ concentrations, the effect of the observations on the optimized surface CO₂ fluxes is important. To investigate the relationship between the information content and the optimized surface CO₂ fluxes, the root mean square differences (RMSDs) between the optimized surface CO₂ fluxes and the background fluxes were calculated (Fig. 13). The surface CO₂ fluxes predicted by the dynamic model in Eq. (2) (i.e., background) show a high RMSD in the NH, with the highest values in North America, followed by Asia (Fig. 13a). In terms of seasonal variation, the impact of the observations in JJA is greater than in DJF (Figs. 13a and b). The large difference between the prior fluxes and the surface CO₂ fluxes predicted by the dynamic model implies that the assimilation of previous observations substantially affects the results. The RMSD of the analyzed surface CO₂ fluxes constrained by one week of observations from the background fluxes in JJA is greater in the NH compared with the other regions. The JJA RMSD value for North America (especially in the mid-continental region of the US) is the highest in the NH (Fig. 13c). Although the RMSD of North America in DJF is lower than that in JJA, the RMSD of North America is still greater than that of other regions in DJF (Fig. 13d). The regions with a high average information content are consistent with the regions with a high RMSD (compare Fig. 9 and Fig. 13), which implies that the observations from North America provide more information in the first cycle than those from other regions because the observations in North America are characterized by high self-sensitivities and abundant observations. By contrast, the RMSD values obtained in the first cycle in other regions are not as high as those in North America. The RMSD in Asia and other regions increases after five weeks of optimization (Figs. 13e and f). In particular, the magnitude of the RMSD in the Eurasian Boreal region increases after five weeks of optimization (Fig. 13e), which implies that, by the transport of the CO₂ concentrations, the observation information from remote regions affects the optimization of the surface CO₂ fluxes in the Eurasian Boreal region. This remote influence is due to the absence of observations in this region. In addition, the five-week assimilation lag is effective in optimizing the surface CO₂ flux in this region. Therefore, a longer, smoother window is necessary to optimize the surface CO₂ flux in Asia, where there are sparse observations; this may imply that in the current version of CarbonTracker, the uncertainty of the surface CO₂

1 flux in Asia may be reduced when using a longer, smoother window than that used for North
2 America. A study on the effect of various assimilation window and ensemble size on the
3 estimation of the surface CO₂ flux in Asia is under way to investigate which lag window and
4 ensemble size are appropriate for Asia in CarbonTracker.

5 **4 Summary and Conclusion**

6 In this study, the effect of observations of CO₂ concentrations on the optimized surface CO₂
7 fluxes in CarbonTracker was evaluated by calculating the influence matrix for a 10-year
8 period from 2000 to 2009. CarbonTracker is a system used to optimize the surface CO₂ flux
9 using EnKF as a data assimilation algorithm. Most of the calculated influence values were in
10 the range of the theoretical limit, from 0 to 1, which makes it possible to objectively diagnose
11 the performance of the data assimilation system used in this study.

12 The average global self-sensitivity is 4.8%, which implies that the impact of the background
13 on the optimized flux is 95.2%. The value of 4.8% obtained in CarbonTracker is lower than
14 the 15% value obtained from NWP models, as reported by Cardinali et al. (2004) and Liu et
15 al. (2009). However, as indicated by Cardinali et al. (2004), the background fluxes predicted
16 by the dynamic model already include information extracted from earlier observations used in
17 previous cycles. Because the state vector used in CarbonTracker includes five weeks of lag,
18 the cumulative impact of the observations on the analysis is greater than the impact calculated
19 for a single assimilation cycle. The cumulative impact over five weeks is 19.1%, much
20 greater than 4.8%, and the large cumulative impact is confirmed by the RMSD of the surface
21 CO₂ fluxes associated with each assimilation process.

22 The self-sensitivity and spatial coverage of the observation sites are inversely correlated in
23 the NH, whereas these factors are not apparently related in the Tropics and SH. The lower
24 correlation between the self-sensitivity and the spatial coverage of the observation sites in the
25 Tropics and SH is attributed to either the sparseness of the observation sites or the locations
26 of the observation sites which are not appropriate for detecting the variability of CO₂
27 concentrations with a high temporal resolution but are appropriate for detecting the global
28 trend of the background CO₂ concentrations. By contrast, the observation sites near the
29 Eurasian Boreal region show high self-sensitivity because there are no available observations
30 in the Eurasian Boreal region.

1 The self-sensitivity time series is characterized by seasonal variations. In both hemispheres,
2 the self-sensitivity in summer is greater than in winter, which is clearly evident in the Mixed
3 and Continuous site categories and is associated with the background surface CO₂ flux
4 uncertainties. The number of observations used in data assimilation increases over time,
5 which causes the average self-sensitivities to decrease. The decreasing trend of the self-
6 sensitivity over time for the Continuous site observations in North America may indicate the
7 limited impact of additional observations in this region. Schuh et al. (2013) reported that
8 additional tower measurements (i.e., observations in the Continuous site category) in the
9 Corn Belt region of the US did not significantly alter the surface CO₂ flux estimates for 2008,
10 which is consistent with the low self-sensitivity detected over North America in the same
11 period. Therefore, under the current CarbonTracker framework, to obtain the beneficial effect
12 of additional observations on the surface CO₂ flux analysis, new observations should be
13 added in regions with a low spatial density of observation sites (e.g., Asia).

14 The observation sites with a high average self-sensitivity and a small number of observations
15 show low average information content, whereas the observation sites with a low average self-
16 sensitivity and a large number of observations show high average information content
17 because the range of average self-sensitivity is bounded from 0 to 1, but the range of the
18 number of observations is large. Therefore, the Continuous site category shows high average
19 information content. In general, the information extracted from observations is concentrated
20 in the NH, especially in North America. A strong correlation exists between the information
21 content and the optimized surface CO₂ fluxes. The high information content found in regions
22 with a large number of observations implies that much of the information is extracted from
23 observations, and as a result, the fluxes are optimized quickly in a relatively short period.
24 However, the surface CO₂ fluxes in regions with no local observation sites (e.g., Siberia) are
25 optimized by remote observations during relatively long assimilation windows with a lag.

26 The effect of various observations on the analyzed surface CO₂ fluxes can be calculated using
27 the method suggested in this study. More CO₂ observations become available in data
28 assimilation for estimating the surface CO₂ fluxes. These additional sources include
29 CONTRAIL data, which are aircraft observations (Machida et al., 2008); column-averaged
30 CO₂ concentrations retrieved from the Japanese Greenhouse gases Observing SATellite
31 (GOSAT) (Yokoda et al., 2009); and data from the Total Carbon Column Observing Network

1 (TCCON), which are observed by ground-based Fourier Transform Spectrometers (Wunch et
2 al., 2011). As a next step, the impact of various observations on the optimization of surface
3 CO₂ fluxes can be evaluated using the method suggested in this study.

4

5 **Acknowledgements**

6 The authors thank the two anonymous reviewers for their valuable comments. The authors
7 thank Dr. Andrew R. Jacobson for providing the resources necessary for this study. This
8 study was funded by the Korea Meteorological Administration Research and Development
9 Program under the Grant CATER 2012-3032.

10

1 **References**

- 2 Anderson, J. I.: Spatially and temporally varying adaptive covariance inflation for ensemble
3 filters, *Tellus*, 61A, 72-83, doi:10.1111/j.1600-0870.2008.00361.x, 2009.
- 4 Baker, D. F., Doney, S. C., and Schimel, D. S.: Variational data assimilation for atmospheric
5 CO₂, *Tellus*, 58B, 359-365, 2006.
- 6 Baker, D. F., Bösch, H., Doney, S. C., O'Brien, D., and Schimel, D. S.: Carbon source/sink
7 information provided by column CO₂ measurements from the Orbiting Carbon Observatory,
8 *Atmos. Chem. Phys.*, 10, 4145-4165, doi:10.5194/acp-10-4145-2010, 2010.
- 9 Basu, S., Guerlet, S., Butz, A., Houweling, S., Hasekamp, O., Aben, I., Krummel, P., Steele,
10 P., Langenfelds, R., Torn, M., Biraud, S., Stephens, B., Andrews, A., and Worthy, D.: Global
11 CO₂ fluxes estimated from GOSAT retrievals of total column CO₂, *Atmos. Chem. Phys.*, 12,
12 86958717, doi:10.5194/acp-13-8695-2013, 2013.
- 13 Bowler, N. E, Arribas, A., Mylne, K. R., Robertson, K. B., and Beare, S. E.: The
14 MOGREPS short-range ensemble prediction system, *Q. J. R. Meteorol. Soc.*, 134, 703-722,
15 2008.
- 16 Bruhwiler, L. M. P., Michalak, A. M., Peters, W., Baker, D. F., and Tans, P.: An improved
17 Kalman Smoother for atmospheric inversions, *Atmos. Chem. Phys.*, 5, 2691-2702, 2005.
- 18 Cardinali, C., Pezzulli S., and Andersson E.: Influence-matrix diagnostic of a data
19 assimilation system, *Q. J. R. Meteorol. Soc.*, 130, 2767-2786, 2004.
- 20 Chatterjee, A., Michalak, A. M., Anderson, J. L., Mueller, K. L., Yadav, V.: Toward reliable
21 ensemble Kalman filter estimates of CO₂ fluxes, *J. Geophys. Res.*, 117, D22306,
22 doi:10.1029/2012JD018176, 2012.
- 23 Chevallier, F., Engelen, R. J., Carouge, C., Conway, T. J., Peylin, P., Pickett-Heaps, C.,
24 Ramonet, M., Rayner, P. J., and Xueref-Remy, I.: AIRS-based versus flask-based estimation
25 of carbon surface fluxes, *J. Geophys. Res.*, 114, D20303, doi:10.1029/2009JD012311, 2009a.
- 26 Chevallier, F., Fisher, M., Peylin, P., Seerrar, S., Bousque, P., Bréon, F.-M., Chédin, A., and
27 Ciais, P.: Inferring CO₂ sources and sinks from satellite observations: Method and application
28 to TOVS data, *J. Geophys. Res.*, 110, D24309, doi:10.1029/2005JD006390, 2005.

1 Chevallier, F., Maksyutov, S., Bousquet, P., Bréon, F.-M., Saito, R., Yoshida, Y., and Yokota,
2 T.: On the accuracy of the CO₂ surface fluxes to be estimated from the GOSAT observations,
3 *Geophys. Res. Lett.*, 36, L19807, doi:10.1029/2009GL040108, 2009b.

4 Ciais P., Rayner, P., Chevallier, F., Bousquet, P., Logan, M., Peylin, P., and Ramonet, M.:
5 Atmospheric inversions for estimating CO₂ fluxes: methods and perspectives, *Climate*
6 *Change*, 103, 69-92, 2010.

7 Engelen R. J., and Stephens, G. L.: Information content of infrared satellite sounding
8 measurements with respect to CO₂, *J. Appl. Meteorol.*, 43, 373–378, 2004.

9 Feng, L., Palmer, P. I., Bosch, H., and Dance, S.: Estimating surface CO₂ fluxes from space-
10 born CO₂ dry air mole fraction observations using an ensemble Kalman Filter, *Atmos. Chem.*
11 *Phys.*, 9, 2619-2633, 2009.

12 Gurney, K. R., Law, R. M., Denning, A. S., Rayner, P. J., Baker, D., Bousquet, P., Bruhwiler,
13 L., Chen, Y. H., Ciais, P., Fan, S., Fung, I. Y., Gloor, M., Heimann, M., Higuchi, K., John, J.,
14 Maki, T., Maksyutov, S., Masarie, K., Peylin, P., Prather, M., Pak, B. C., Randerson, J.,
15 Sarmiento, J., Taguchi, S., Takahashi, T., and Yuen, C. W.: Towards robust regional
16 estimates of CO₂ sources and sinks using atmospheric transport models, *Nature*, 415, 626–
17 630, 2002.

18 Houtekamer, P. L., and H. L., Mitchell, A sequential ensemble Kalman filter for atmospheric
19 data assimilation, *Mon. Wea. Rev.*, 129, 123-137, 2001.

20 Jacobson, A. R., Fletcher, S. E. M., Gruber, N., Sarmiento, J. L., and Gloor, M.: A joint
21 atmosphere-ocean inversion for surface fluxes of carbon dioxide: 2. Regional results, *Glob.*
22 *Biogeochem. Cycles*, 21, GB1019, doi:10.1029/2006GB002703, 2007.

23 Kang, J. S., Kalnay, E., Liu, J., Fung, I., Miyoshi, T., and Ide, K.: “Variable localization” in
24 an ensemble Kalman filter: Application to the carbon cycle data assimilation, *J. Geophys.*
25 *Res.*, 116, D09110, doi:10.1029/2010JD014673, 2011

26 Kang, J. S., Kalnay, E., Miyoshi, T., Liu, J., and Fung, I.: Estimation of surface carbon fluxes
27 with an advanced data assimilation methodology, *J. Geophys. Res.*, 117, D24101,
28 doi:10.1029/2012JD018259, 2012.

- 1 Kim, J., Kim, H. M., and Cho, C.-H.: Application of Carbon Tracking System based on
2 ensemble Kalman Filter on the diagnosis of Carbon Cycle in Asia, *Atmosphere*, 22(4), 415-
3 447, 2012. (in Korean with English abstract)
- 4 Kim, J., Kim, H. M., and Cho, C.-H.: The effect of optimization and the nesting domain on
5 carbon flux analyses in Asia using a carbon tracking system based on the ensemble Kalman
6 filter, *Asia-Pacific J. Atmos. Sci.*, 50, 327–344, doi:10.1007/s13143-014-0020-y, 2014.
- 7 Krol, M., Houweling, S., Bregman, B., Broek, M., van der Segers, A., Velthoven, P. V.,
8 Peters, W., Dentener, F., and Bergamaschi, P.: The two-way nested global chemistry-
9 transport zoom model TM5: Algorithm and applications, *Atmos. Chem. Phys.*, 5, 417-432,
10 2005.
- 11 Li, H., Kalnay, E., and Miyoshi, T.: Simultaneous estimation of covariance inflation and
12 observation errors within an ensemble Kalman filter, *Q. J. R. Meteorol. Soc.*, 135, 523-533,
13 2009.
- 14 Liu, J, Kalnay, E., Miyoshi, T., and Cardinali, C.: Analysis sensitivity calculation in an
15 ensemble Kalman filter, *Q. J. R. Meteorol. Soc.*, 135, 1842-1851, 2009.
- 16 Lokupitiya, R., S., Zupanski, D., Denning, A. S., Kawa, S. R., Gurney, R., and Zupanski, M.:
17 Estimation of global CO₂ fluxes at regional scale using the maximum likelihood ensemble
18 filter, *J. Geophys. Res.*, 113, D20110, doi:10.1029/2007JD009679, 2008.
- 19 Machida, T., Matsueda, H., Sawa, Y., Nakagawa, Y., Hirotani, K., Kondo, N., Goto, K.,
20 Nakazawa, T., Ishikawa, K., and Ogawa, T.: Worldwide measurements of atmospheric CO₂
21 and other trace gas species using commercial airlines, *J. Atmos. Oceaninc. Technol.*, 25,
22 1744-1754, doi:10.1175/2008JTECHA1082.1, 2008.
- 23 Masarie, K. A., Pétron, G., Andrews, A., Bruhwiler, L., Conway, T. J., Jacobson, A. R.,
24 Miller, J. B., Tans, P. P., Worthy, D. E., and Peters, W.: Impact of CO₂ measurement bias on
25 CarbonTracker surface flux estimates, *J. Geophys. Res.*, 116, D17305,
26 doi:10.1029/2011JD016270, 2011.
- 27 Meirink, J. F., Bergamaschi, P., Frankenberg, C., d’Amelio, M. T. S., Dlugokencky, E. J.,
28 Gatti, L. V., Houweling, S., Miller, J. B., Röckmann, T., Villani, M. G., and Krol, M. C.:
29 Four-dimensional variational data assimilation for inverse modeling of atmospheric methane

1 emissions: Analysis of SCIAMACHY observations, *J. Geophys. Res.*, 113, D17301,
2 doi:10.1029/2007JD009740, 2008.

3 Miyazaki, K., Maki, T., Patra, P., and Nakazawa, T.: Assessing the impact of satellite, aircraft,
4 and surface observations on CO₂ flux estimation using an ensemble-based 4-D data
5 assimilation system, *J. Geophys. Res.*, 116, D16306, doi:10.1029/2010JD015366, 2011.

6 Miyoshi, T.: The Gaussian approach to adaptive covariance inflation and its implementation
7 with the local ensemble transform Kalman filter, *Mon. Wea. Rev.*, 139, 1519-1535,
8 doi:10.1175/2010MWR3570.1, 2011.

9 Talagrand O.: Assimilation of observations, an introduction. *J. Meteorol Soc. Jpn.*, 75, 191-
10 209, 1997.

11 Peters, W., Miller, J. B., Whitaker, J., Denning, A. S., Hirsch, A., Krol, M. C., Zupanski, D.,
12 Bruhwiler, L., and Tans, P. P.: An ensemble data assimilation system to estimate CO₂ surface
13 fluxes from atmospheric trace gas observations, *J. Geophys. Res.*, 110, D24304,
14 doi:10.1029/2005JD006157, 2005.

15 Peters, W., Jacobson, A. R., Sweeney, C., Andrews, A. E., Conway, T. J., Masarie, K., Miller,
16 J. B., Bruhwiler, L. M. P., Petron, G., Hirsch, A. I., Worthy, D. E. J., van der Werf, G. R.,
17 Randerson, J. T., Wennberg, P. O., Krol, M. C., Tans, P. P.: An atmospheric perspective on
18 North American carbon dioxide exchange: CarbonTracker, *Proc. Nat. Acad. Sci. U.S.A.*, 104,
19 18925-18930, 2007.

20 Peters, W., Krol, M. C., van der Werf, G. R., Houweling, S., Jones, C. D., Hughes, J.,
21 Schaefer, K., Masarie, K. A., Jacobson, A. R. Miller, J. B., Cho, C. H., Ramonet, M.,
22 Schmidt, M., Ciattaglia, L., Apadula, F., Heltai, D., Meinhardt, F., di Sarra, A. G., Piacentino,
23 S., Sferlazzo, D., Aalto, T., Hatakka, J., Ström, J., Haszpra, L., Meijer, H. A. J., van der Laan,
24 S., Neubert, R. E. M., Jordan, A., Rodó, X., Morguí, J. A., Vermeulen, A. T., Popa, E.,
25 Rozanski, K., Zimnoch, M., Manning, A. C., Leuenberger, M., Uglietti, C., Dolman, A. J.,
26 Ciais, P. Heimann, M., and Tans, P. P.: Seven years of recent European net terrestrial carbon
27 dioxide exchange constrained by atmospheric observations, *Global Change Biol.*, 16, 1317-
28 1337, doi:10.1111/j.1365-2486.2009.02078.x, 2010.

1 Peylin P., Law, R. M., Gurney, K. R., Chevallier, F., Jacobson A. R., Maki, T., Niwa, Y.,
2 Patra, P. K., Peters, W., Rayner, P. J., Rödenbeck, C., van der Laan-Luijkx, I. T., and Zhang,
3 X.: Global atmospheric carbon budget: results from an ensemble of atmospheric CO₂
4 inversions, *Biogeosciences*, 10, 6699-6720, doi:10.5194/bg-10-6699-2013, 2013.

5 Rodgers, C. D.: *Inverse Methods for Atmospheric Sounding*, World Scientific, London, 2000.

6 Schuh, A. E., Lauvaux, T., West, T. O., Denning, A. S., Dvais, K. J., Miles, N., Richardson,
7 S., Uliasz, M., Lokupitiya, E., Cooley, D., Andrews, A., and Ogle S.: Evaluating atmospheric
8 CO₂ inversions at multiple scales over a highly inventoried agricultural landscape, *Global*
9 *Change. Biol.*, 19, 1424-1439, doi:10.1111/gcb.12141, 2013.

10 Wang, X., and Bishop, C. H.: A comparison of breeding and ensemble transform Kalman
11 filter ensemble forecast schemes, *J. Atmos. Sci.*, 60, 1140-1158, 2003.

12 van der Werf, G. R., Randerson, J. T., Giglio, L., Collatz, G. J., Mu, M., Kasibhatla, P. S.,
13 Morton, D. C., DeFries, R. S., Jin, Y., and van Leeuwen, T. T.: Global fire emissions and the
14 contribution of deforestation, savanna, forest, agricultural, and peat fires (1997–2009), *Atmos.*
15 *Chem. Phys.*, 10, 11707–11735, doi:10.5194/acp-10-11707-2010, 2010.

16 Whitaker, J. S., and Hamill, T. M.: Ensemble Data Assimilation without Perturbed
17 Observations, *Mon. Wea. Rev.*, 130, 1913-1924, 2002.

18 Whitaker, J. S., Hamill, T. M., Wei, X., Song, Y., and Toth, Z.: Ensemble data assimilation
19 with the NCEP global forecast system, *Mon. Wea. Rev.*, 136, 463-482,
20 doi:10.1175/2007MWR2018.1, 2008.

21 Wunch, D., Toon, G. C., Wennberg, P. O., Wofsy, S. C., Stephens, B. B., Fischer, M. L.,
22 Uchino, O., Abshire, J. B., Bernath, P., Biraud, S. C., Blavier, J.-F. L., Boone, C., Bowman,
23 K. P., Browell, E. V., Campos, T., Connor, B. J., Daube, B. C., Deutscher, N. M., Diao, M.,
24 Elkins, J. W., Gerbig, C., Gottlieb, E., Griffith, D. W. T., Hurst, D. F., Jim´enez, R., Keppel-
25 Aleks, G., Kort, E. A., Macatangay, R., Machida, T., Matsueda, H., Moore, F., Morino, I.,
26 Park, S., Robinson, J., Roehl, C. M., Sawa, Y., Sherlock, V., Sweeney, C., Tanaka, T., and
27 Zondlo, M. A.: Calibration of the Total Carbon Column Observing Network using aircraft
28 profile data, *Atmos. Meas. Tech.*, 3, 1351–1362, doi:10.5194/amt-3-1351-2010, 2010.

- 1 Yokota, T., Yoshida, Y., Eguchi, N., Ota, Y., Tanaka, T., Watanabe, H., Maksyutov, S.:
2 Global Concentrations of CO₂ and CH₄ Retrieved from GOSAT: First Preliminary Results,
3 *Sci. Online. Lett. Atmos.*, 5, 160-163, doi:10.2151/sola.2009-041, 2010.
- 4 Zhang, H. F., Chen, B. Z. , van der Laan-Luijkx, I. T., Machida, T., Matsueda, H., Sawa, Y.,
5 Fukuyama, Y., Langenfelds, R., van der Schoot, M., Xu, G., Yan, J. W., Cheng, M. L., Zhou,
6 X., Tans, P. P., and Peters, W.: Estimating Asian terrestrial carbon fluxes from CONTRAIL
7 aircraft and surface CO₂ observations for the period 2006-2010, *Atmos. Chem. Phys.*, 14,
8 5807-5824, doi:10.5194/acp-14-5807-2014, 2014.
- 9 Zupanski, D., Denning, A. S., Uliasz, M., Zupanski, M., Schuh, A. E, Rayner, P. J, Peters, W.,
10 and Corbin, K. D.: Carbon flux bias estimation employing Maximum Likelihood Ensemble
11 Filter (MLEF), *J. Geophys. Res.*, 112, D17107, 2007.

1 Table 1. Information on the observation sites used in this study. MDM represents the model-data mismatch, which is the observation error.

Site code	Location	Latitude	Longitude	Height	Laboratory	MDM [ppm]
ALT_01D0	Alert, Nunavut, Canada	82.45°N	62.51°W	200 m	ESRL	1.5
ALD_06C0	Alert, Nunavut, Canada	82.45°N	62.51°W	200 m	ESRL	2.5
AMT_01C3	Argyle, Maine, United States	45.03°N	68.68°W	50 m	ESRL	3
AMT_01P0	Argyle, Maine, United States	45.03°N	68.68°W	50 m	ESRL	3
ASC_01D0	Ascension Island, United Kingdom	7.92°S	14.42°W	54 m	ESRL	0.75
ASK_01D0	Assekrem, Algeria	23.18°N	5.42°E	2728 m	ESRL	1.5
AZR_01D0	Terceira Island, Azores, Portugal	38.77°N	27.38°W	40 m	ESRL	1.5
BAL_01D0	Baltic Sea, Poland	55.35°N	17.22°E	3 m	ESRL	7.5
BAO_01C3	Boulder Atmospheric Observatory, Colorado, United States	40.05°N	105.00°W	1584 m	ESRL	3
BAO_01P0	Boulder Atmospheric Observatory, Colorado, United States	40.05°N	105.00°W	1584 m	ESRL	3
BKT_01D0	Bukit Kotobang, Indonesia	0.20°S	100.32°E	864 m	ESRL	7.5
BME_01D0	St. Davids Head, Bermuda, United Kingdom	32.27°N	64.65°E	30 m	ESRL	1.5

BMW_01D0	Tudor Hill, Bermuda, United Kingdom	32.27°N	64.88°E	30 m	ESRL	1.5
BRW_01D0	Barrow, Alaska, United States	71.32°N	156.61°W	11 m	ESRL	1.5
BRW_01C0	Barrow, Alaska, United States	71.32°N	156.61°W	11 m	ESRL	2.5
BSC_01D0	Black Sea, Constanta, Romania	44.17°N	28.68°E	3 m	ESRL	7.5
CBA_01D0	Cold Bay, Alaska, United States	55.21°N	162.72°W	21 m	ESRL	1.5
CDL_06C0	Candle Lake, Saskatchewan, Canada	53.99°N	105.12°W	600 m	ESRL	3
CFA_02D0	Cape Ferguson, Queensland, Australia	19.28°S	147.06°E	184 m	ESRL	2.5
CGO_01D0	Cape Grim, Tasmania, Australia	40.68°S	144.69°E	94 m	ESRL	0.75
CGO_02D0	Cape Grim, Tasmania, Australia	40.68°S	144.69°E	94 m	CSIRO	0.75
CHR_01D0	Christmas Island, Republic of Kiribati	1.70°N	157.17°W	3 m	ESRL	0.75
CRZ_01D0	Crozet Island, France	46.45°S	51.85°E	120 m	ESRL	0.75
cya_02D0	Casey, Antarctica, Australia	66.28°S	110.5°E	51 m	CSIRO	0.75
EGB_06C0	Egbert, Ontario, Canada	44.23°N	79.78°W	251 m	EC	3
EIC_01D0	Easter Island, Chile	27.15°S	109.45°W	50 m	ESRL	7.5
ESP_06C0	Estevan Point, British Columbia, Canada	49.38°N	126.54°W	7 m	EC	3

ETL_06C0	East Trout Lake, Saskatchewan, Canada	54.35°N	104.98°W	492 m	EC	3
FEF_03C0	Fraser, Colorado, United States	39.91°N	105.88°W	2745 m	NCAR	3
FSD_06C0	Fraserdale, Canada	49.88°N	81.57°W	210 m	EC	3
GMI_01D0	Mariana Islands, Guam	13.43°N	144.78°E	2 m	ESRL	1.5
HBA_01D0	Halley Station, Antarctica, United Kingdom	75.58°S	26.50°W	30 m	ESRL	0.75
HDP_03C0	Hidden Peak (Snowbird), Utah, United States	40.56°N	111.65°W	3351 m	NCAR	3
HUN_01D0	Hegyhatsal, Hungary	46.95°N	16.65°E	248 m	ESRL	7.5
ICE_01D0	Storhofdi, Vestmannaeyjar, Iceland	63.40°N	20.29°W	118 m	ESRL	1.5
KEY_01D0	Key Biscayne, Florida, United States	25.67°N	80.16°W	3 m	ESRL	2.5
KUM_01D0	Cape Kumukahi, Hawaii, United States	19.52°N	154.82°W	3 m	ESRL	1.5
KZD_01D0	SaryTaukum, Kazakhstan	44.06°N	76.82°E	601 m	ESRL	2.5
KZM_01D0	Plateau Assy, Kazakhstan	43.25°N	77.88°E	2519 m	ESRL	2.5
LEF_01C3	Park Falls, Wisconsin, United States	45.95°N	90.27°W	472 m	ESRL	3
LEF_01P0	Park Falls, Wisconsin, United States	45.95°N	90.27°W	472 m	ESRL	3
LLB_06C0	Lac La Biche, Alberta, Canada	54.95°N	112.45°W	540 m	EC	3

MAA_02D0	Mawson Station, Antarctica, Australia	67.62°S	62.87°E	32 m	CSIRO	0.75
MHD_01D0	Mace Head, County Galway, Ireland	53.33°N	9.90°W	5 m	ESRL	2.5
MID_01D0	Sand Island, Midway, United States	28.21°N	177.38°W	4 m	ESRL	1.5
MKN_01D0	MT. Kenya, Kenya	0.05°S	37.30°E	3897 m	ESRL	2.5
MLO_01C0	Mauna Loa, Hawaii, United States	19.54°N	155.58°W	3397 m	ESRL	0.75
MLO_01D0	Mauna Loa, Hawaii, United States	19.54°N	155.58°W	3397 m	ESRL	1.5
MNM_19C0	Minamitorishima, Japan	24.29°N	153.98°E	8 m	JMA	3
MQA_02D0	Macquarie Island, Australia	54.48°S	158.97°E	12 m	CSIRO	0.75
NMB_01D0	Gobabeb, Namibia	23.58°S	15.03°E	456 m	ESRL	2.5
NWR_01D0	Niwot Ridge, Colorado, United States	40.05°N	105.58°W	3523 m	ESRL	1.5
NWR_03C0	Niwot Ridge, Colorado, United States	40.05°N	105.58°W	3523 m	NCAR	3
OBN_01D0	Obninsk, Russia	55.11°N	36.60°E	183 m	ESRL	7.5
OXK_01D0	Ochsenkopf, Germany	50.03°N	11.80°E	1022 m	ESRL	2.5
PAL_01D0	Pallas-Sammaltunturi, GAW Station, Germany	67.97°N	24.12°E	560 m	ESRL	2.5
POC_01D1	Pacific Ocean, N/A	0.39°S	132.43°W	10 m	ESRL	0.75

PSA_01D0	Palmer Station, Antarctica, United States	64.92°S	64.00°W	10 m	ESRL	0.75
PTA_01D0	Point Arena, California, United States	38.95°N	123.74°W	17 m	ESRL	7.5
RPB_01D0	Ragged Point, Barbados	13.17°N	59.43°W	45 m	ESRL	1.5
RYO_19C0	Ryori, Japan	39.03°N	141.82°E	260 m	JMA	3
SCT_01C3	Beech Island, South Carolina, United States	33.41°N	81.83°W	115 m	ESRL	3
SEY_01D0	Mahe Island, Seychelles	4.67°S	55.17°E	3 m	ESRL	0.75
SGP_01D0	Southern Great Plains, Oklahoma, United States	36.80°N	97.50°W	314 m	ESRL	2.5
SGP_64C3	Southern Great Plains, Oklahoma, United States	36.80°N	97.50°W	314 m	ESRL	3
SHM_01D0	Shemya Island, Alaska, United States	52.72°N	174.10°E	40 m	ESRL	2.5
SMO_01C0	Tutuila, American Samoa	14.25°S	170.56°W	42 m	ESRL	0.75
SMO_01D0	Tutuila, American Samoa	14.25°S	170.56°W	42 m	ESRL	1.5
SNP_01C3	Shenandoah National Park, United States	38.62°N	78.35°W	1008 m	ESRL	3
SPL_01C3	Storm Peak Laboratory (Desert Research Institute), United States	40.45°N	106.73°W	3210 m	NCAR	3
SPO_01C0	South Pole, Antarctica, United States	89.98°S	24.80°W	2810 m	ESRL	0.75

SPO_01D0	South Pole, Antarctica, United States	89.98°S	24.80°W	2810 m	ESRL	1.5
STM_01D0	Ocean Station M, Norway	66.00°N	2.00°E	0 m	ESRL	1.5
STR_01P0	Sutro Tower, San Francisco, California, United States	37.76°N	122.45°W	254 m	ESRL	3
SUM_01D0	Summit, Greenland	72.57°N	38.48°W	3238 m	ESRL	1.5
SYO_01D0	Syowa Station, Antarctica, Japan	69.00°S	39.58°E	11 m	ESRL	0.75
TAP_01D0	Tae-ahn Peninsula, Republic of Korea	36.73°N	126.13°E	20 m	ESRL	5
TDF_01D0	Tierra Del Fuego, Ushuaia, Argentina	54.87°S	68.48°W	20 m	ESRL	0.75
THD_01D0	Trinidad head, California, United States	41.73°N	91.35°W	107 m	ESRL	2.5
UTA_01D0	Wendover, Utah, United States	39.90°N	113.72°W	1320 m	ESRL	2.5
UUM_01D0	Ulaan Uul, Mongolia	44.45°N	111.10°E	914 m	ESRL	2.5
WBI_01C3	West Branch, Iowa, United States	41.73°N	91.35°W	242 m	ESRL	3
WBI_01P0	West Branch, Iowa, United States	41.73°N	91.35°W	242 m	ESRL	3
WGC_01C3	Walnut Grove, California, United States	38.27°N	121.49°W	0 m	ESRL	3
WGC_01P0	Walnut Grove, California, United States	38.27°N	121.49°W	0 m	ESRL	3
WIS_01D0	WIS Station, Negev Desert, Israel	31.13°N	34.88°E	400 m	ESRL	2.5

WKT_01C3	Moody, Texas, United States	31.32°N	97.33°W	251 m	ESRL	3
WKT_01C3	Moody, Texas, United States	31.32°N	97.33°W	251 m	ESRL	3
WLG_01D0	Mt. Waliguan, Peoples Republic of China	36.29°N	100.90°E	3810 m	ESRL	1.5
WSA_06C0	Sable Island, Nova Scotia, Canada	49.93°N	60.02°E	5 m	EC	3
YON_19C0	Yonagunijima, Japan	24.47°N	123.02°E	30 m	JMA	3
ZEP_01D0	Ny-Alesund, Svalbard, Norway and Sweden	78.90°N	11.88°E	475 m	ESRL	1.5

1 Table 2. Observation site categories and corresponding MDM values.

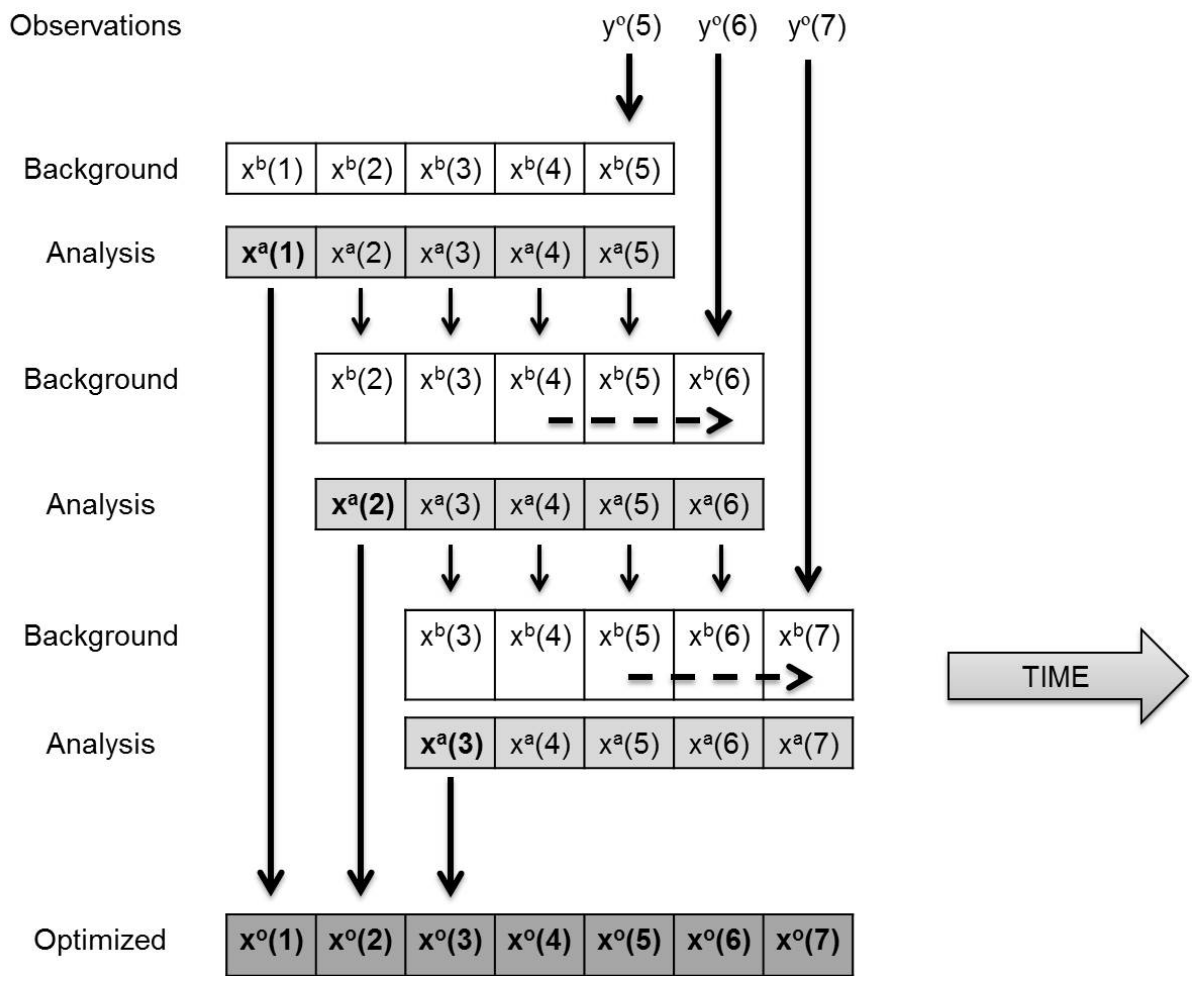
Observation category	Description	Observation frequency	MDM [ppm]
Marine Boundary Layer (MBL)	Observation site close to Marine boundary layer	Once a week	0.75
Mixed land/ocean and mountain (Mixed)	Observation site located in mixed land, ocean, and mountain	Once a week	1.5
Continental	Observation site located in the continent	Once a week	2.5
Continuous	Observation site with continuous observations	Once a day	3
Difficult	Difficult	Once a week	7.5 (5.0)

2

1 Table 3. Information on the observation sites located in Asia, including the number of
 2 observations, number of rejected observations, MDM values, innovation χ^2 statistics, and the
 3 average bias of the model CO₂ concentrations calculated by optimized fluxes. For the
 4 TAP_01D0 site, the numbers in parentheses are values used in previous studies, and the
 5 numbers without parentheses are the modified values based on the innovation χ^2 statistics in
 6 this study.

Site name	Number of observations	Number of rejected observations	MDM	Innovation χ^2	Bias of model CO ₂ concentration
BKT_01D0	207	0	7.5	0.57	-4.01
KZD_01D0	430	11	2.5	1.25	-0.4
KZM_01D0	384	9	2.5	1.22	-0.67
MNM_19C0	3304	0	3	0.16	-0.45
RYO_19C0	3149	108	3	0.53	-0.9
TAP_01D0	339 (269)	10 (3)	5 (7.5)	0.59 (0.37)	0.01 (-0.26)
UUM_01D0	454	10	2.5	1.03	0.26
WIS_01D0	489	3	2.5	0.72	-0.15
WLG_01D0	347	10	1.5	1.14	0.04
YON_19C0	2947	8	3	0.53	-0.9

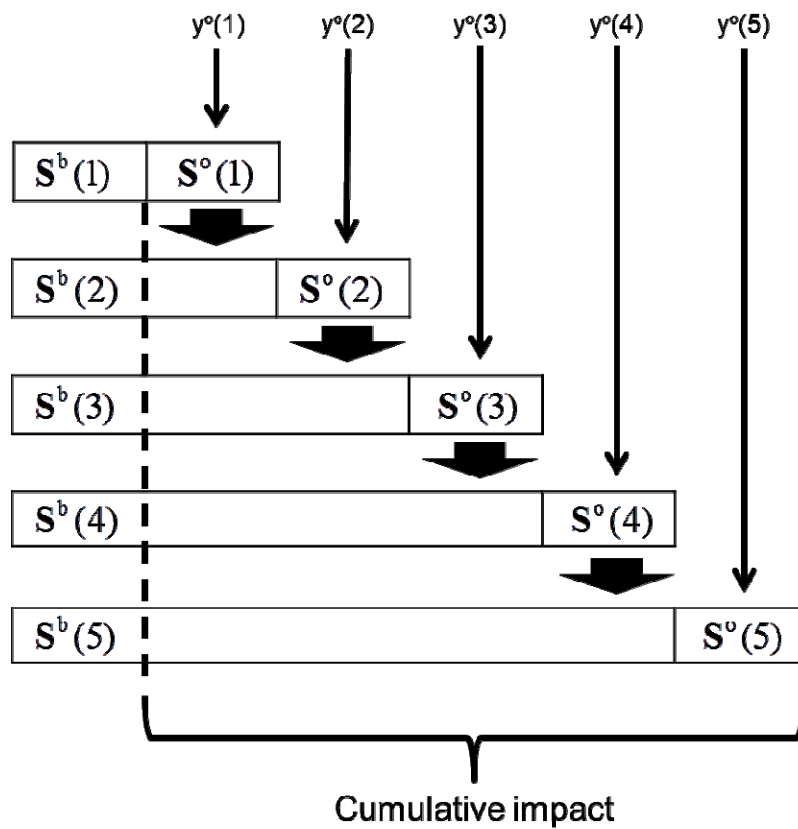
7



1

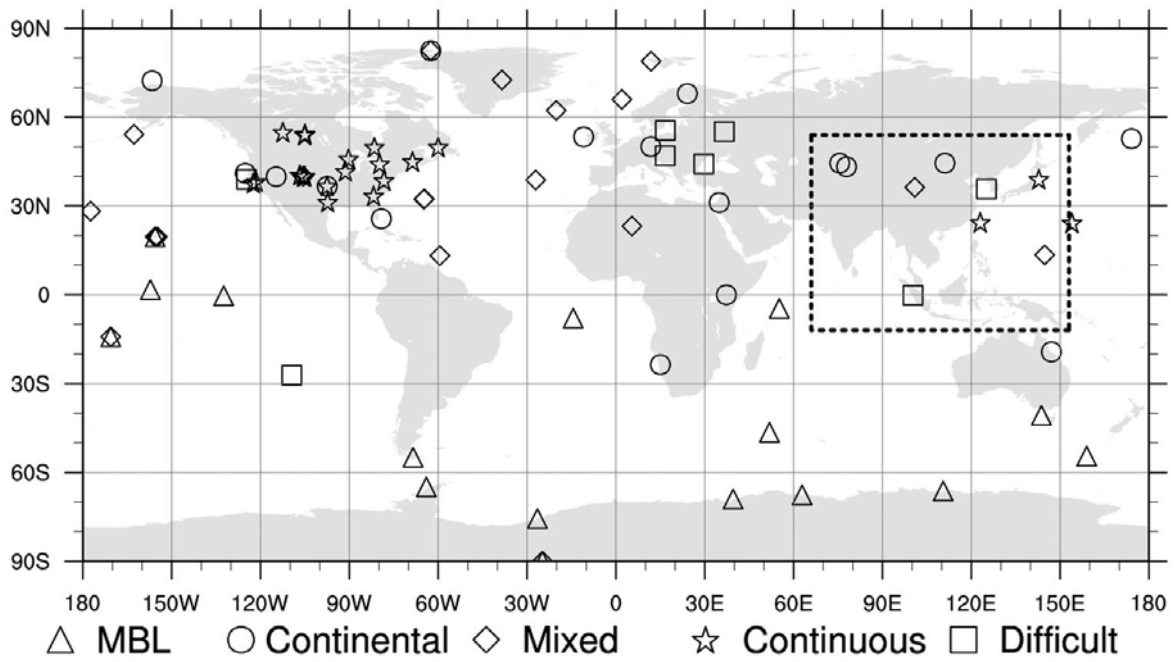
2

3 Figure 1. Schematic diagram of the assimilation process employed in CarbonTracker. In each
 4 analysis cycle, observations made within one week are used to update the state vectors with a
 5 five-week lag. The dashed line indicates how the simple dynamic model uses analysis state
 6 vectors from the previous one and two weeks to produce a new background state vector for
 7 the current analysis time. The TM5 model is used as the observation operator to calculate the
 8 model CO₂ concentration for each corresponding observation location and time.



1
2
3
4
5
6
7

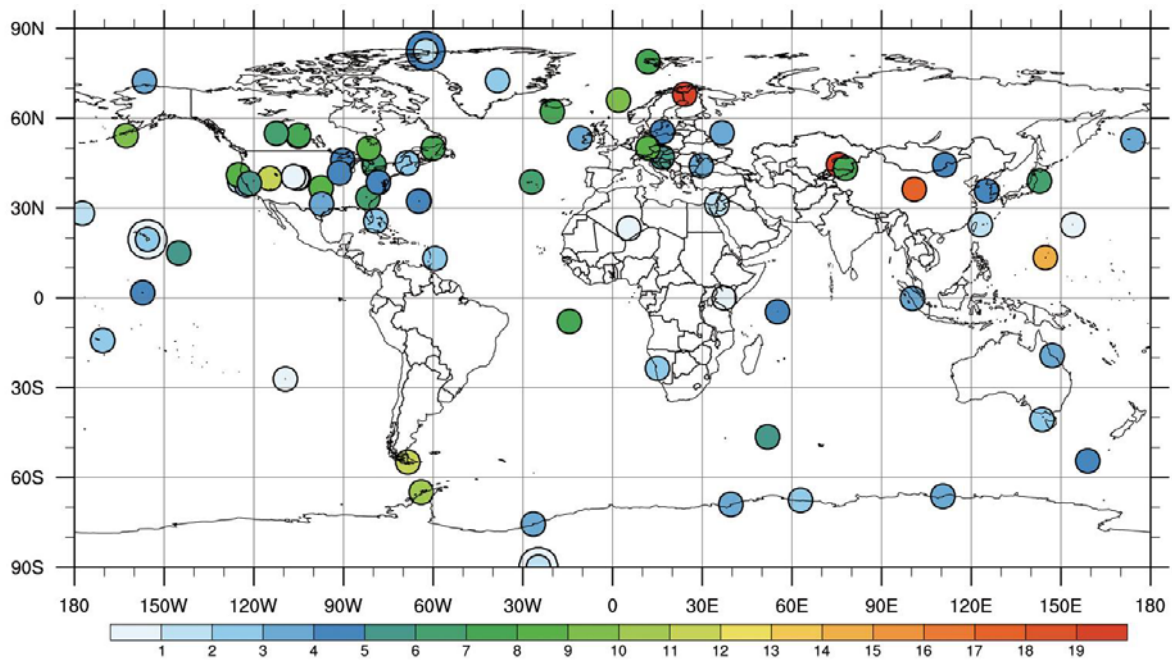
Figure 2. Schematic diagram of calculating cumulative impact in CarbonTraker. $S^b(\bullet)$ indicates the analysis sensitivity to background at each analysis cycle within five weeks of lag, where \bullet denotes each week from 1 to 5. $S^o(\bullet)$ indicates the analysis sensitivity to observation at each analysis cycle.



2

3 Figure 3. Observation network of CO₂ concentrations around the globe and the nested domain
 4 of the TM5 transport model over Asia (dashed box). Each observation site is assigned to
 5 different categories (△: MBL; ○: Continental; ◇: Mixed land/ocean and mountain; ☆:
 6 Continuous; □: Difficult).

7

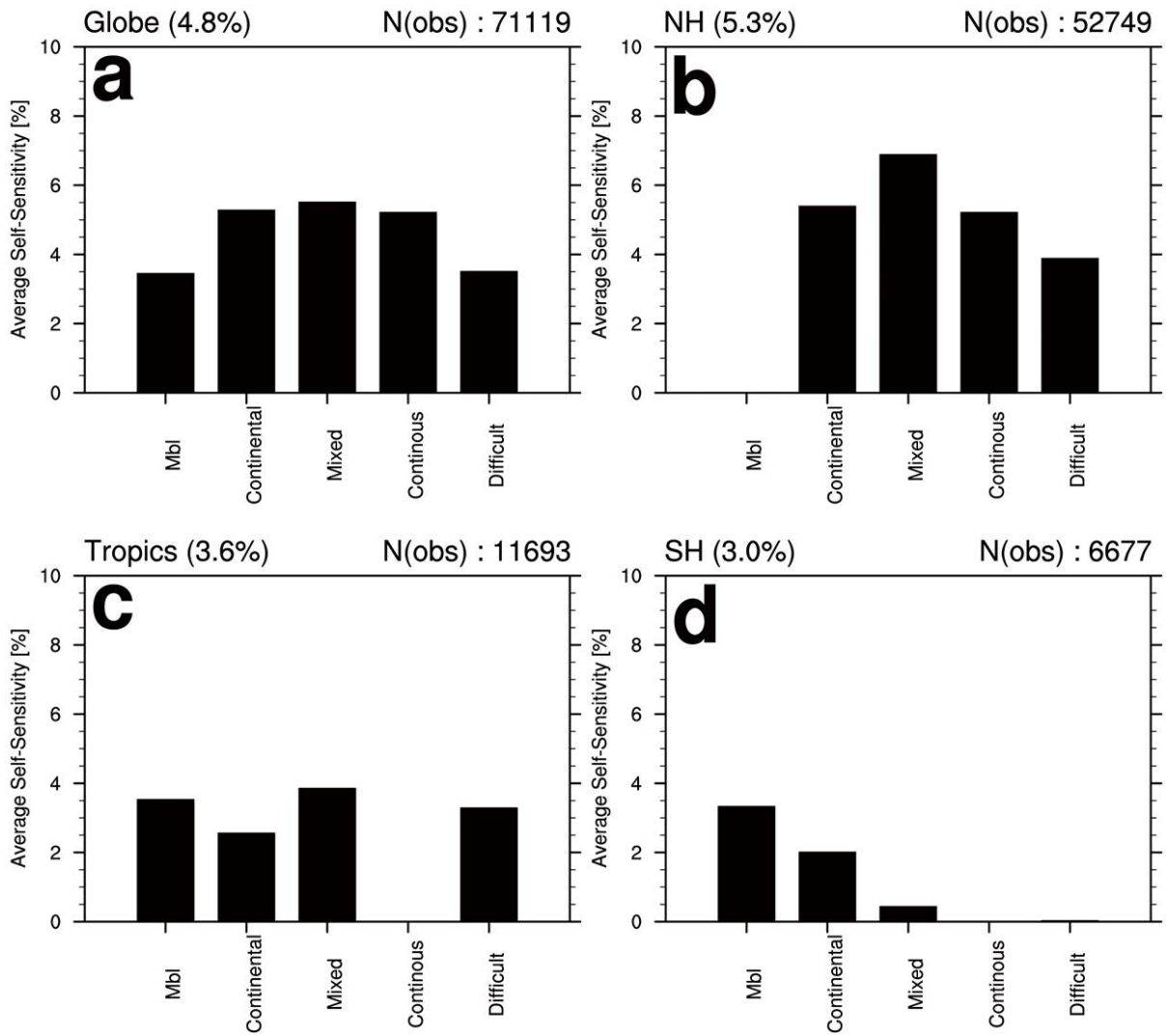


1

2

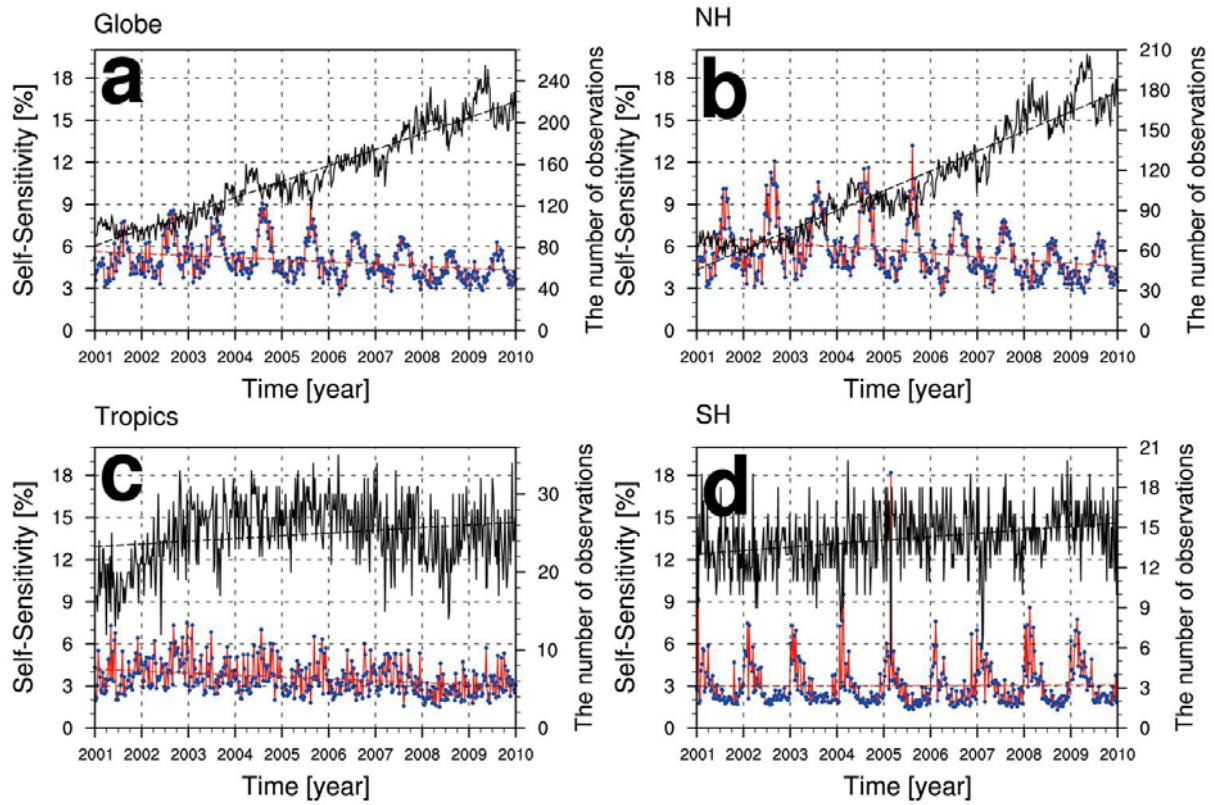
3 Figure 4. Average self-sensitivity at each observation site from 2000 to 2009. The
 4 overlapping observation sites at the same locations or at close locations are distinguished by
 5 different sizes of circles.

6



1
2
3
4
5
6
7

Figure 5. Histograms of the average self-sensitivity for each observation site category from 2000 to 2009 (a) around the globe and in the (b) Northern Hemisphere, (c) Tropics, and (d) Southern Hemisphere. N(obs) in the upper right corner represents the number of observations used in data assimilation.

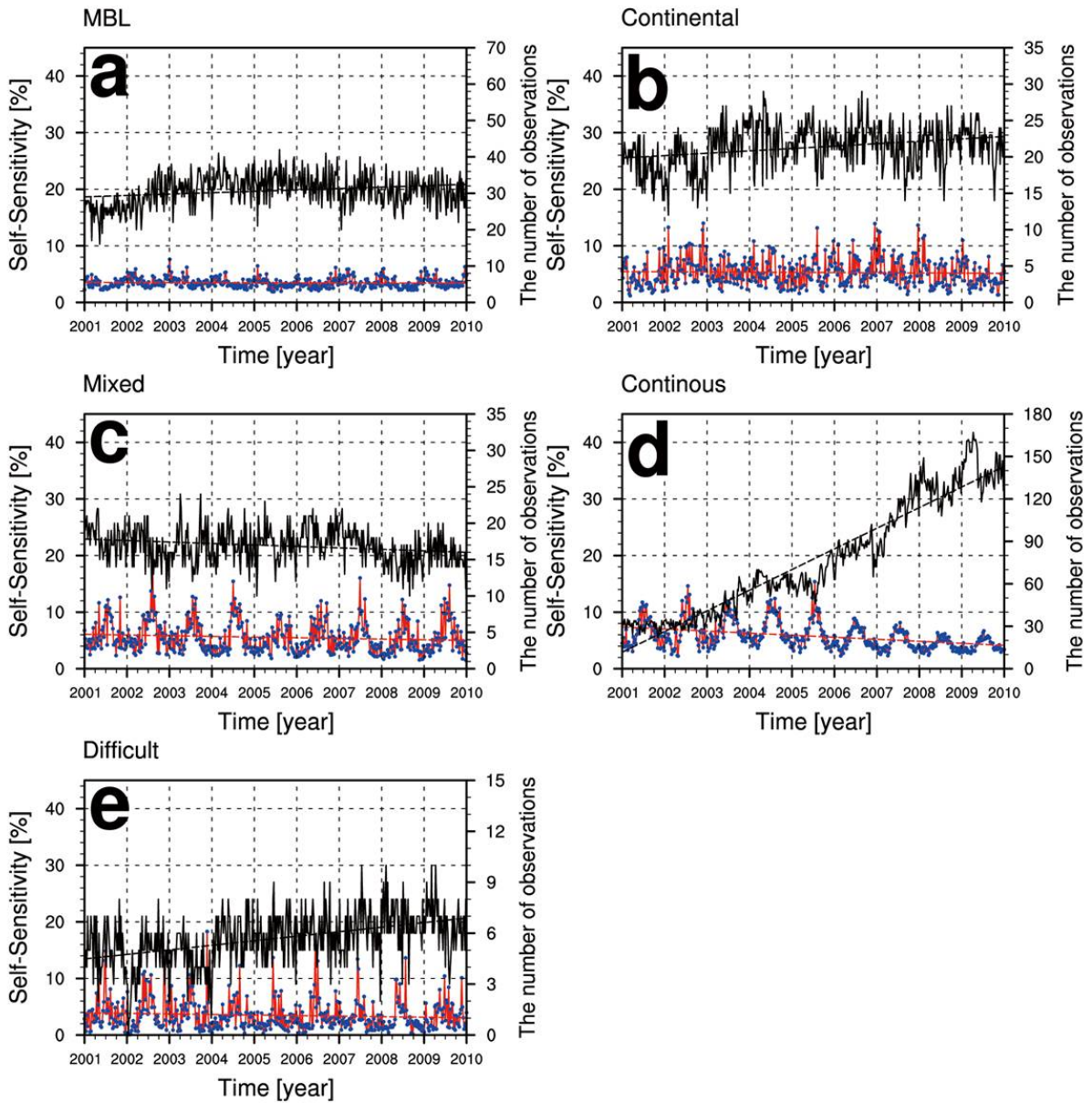


1

2

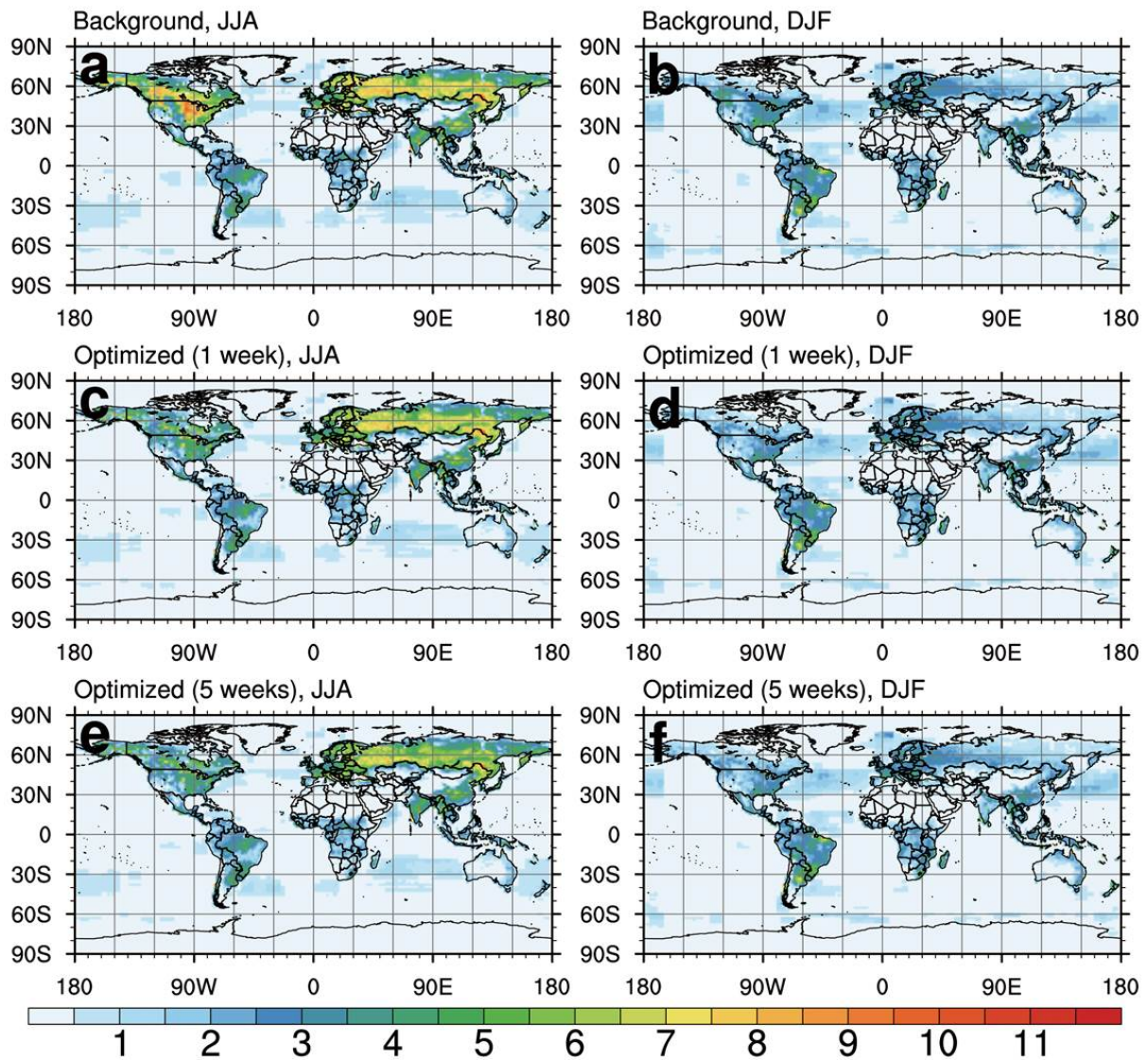
3 Figure 6. Time series of the average self-sensitivity (red solid line with blue dots) and the
 4 number of observations (black solid line) with a weekly temporal resolution (a) around the
 5 globe and in the (b) Northern Hemisphere, (c) Tropics, and (d) Southern Hemisphere from
 6 2000 to 2009. The dashed lines represent the regression lines for the average self-sensitivity
 7 (red dashed line) and the number of observations (black dashed line).

8



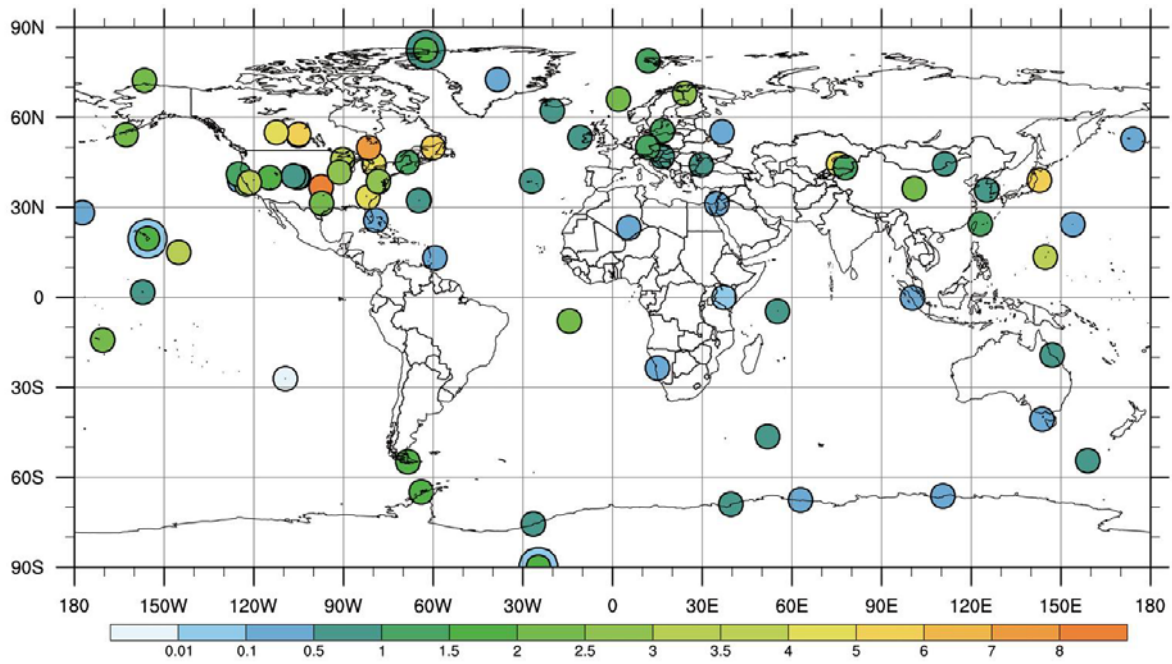
1
2
3
4
5
6
7
8

Figure 7. Time series of the average self-sensitivity (red solid line with blue dots) and the number of observations (black solid line) with a weekly temporal resolution for the (a) MBL, (b) Continental, (c) Mixed, (d) Continuous, and (e) Difficult observation site categories from 2000 to 2009. The dashed lines represent the regression lines for the average self-sensitivity (red dashed line) and the number of observations (black dashed line).



1
2
3
4
5
6
7

Figure 8. Average standard deviation of background biosphere and ocean fluxes in (a) JJA and (b) DJF; the posterior biosphere and ocean fluxes optimized by one-week observations in (c) JJA and (d) DJF; and the posterior biosphere and ocean fluxes optimized by five weeks of observations in (e) JJA and (f) DJF. The units are $\text{g C m}^{-2} \text{ week}^{-1}$.

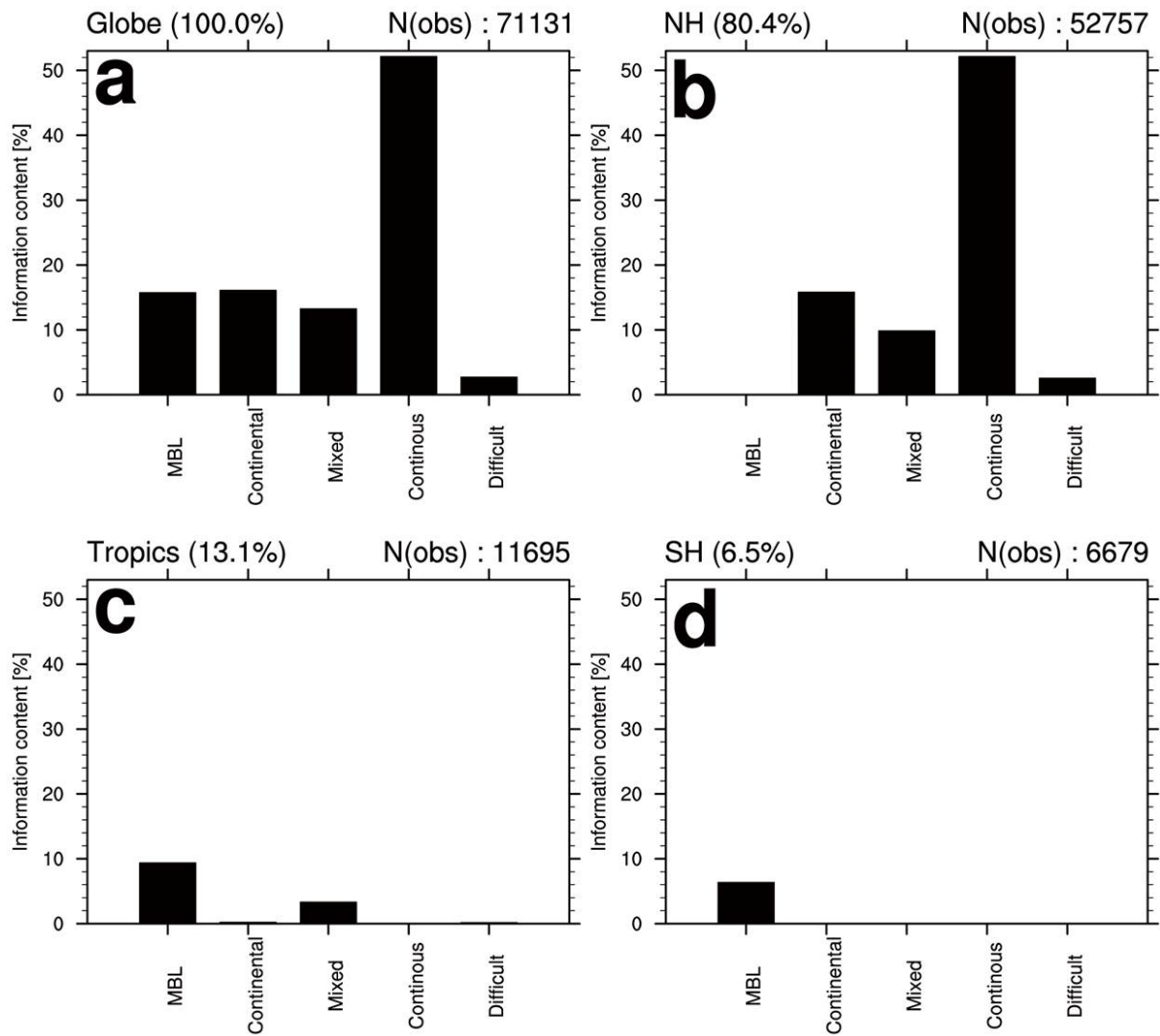


1

2

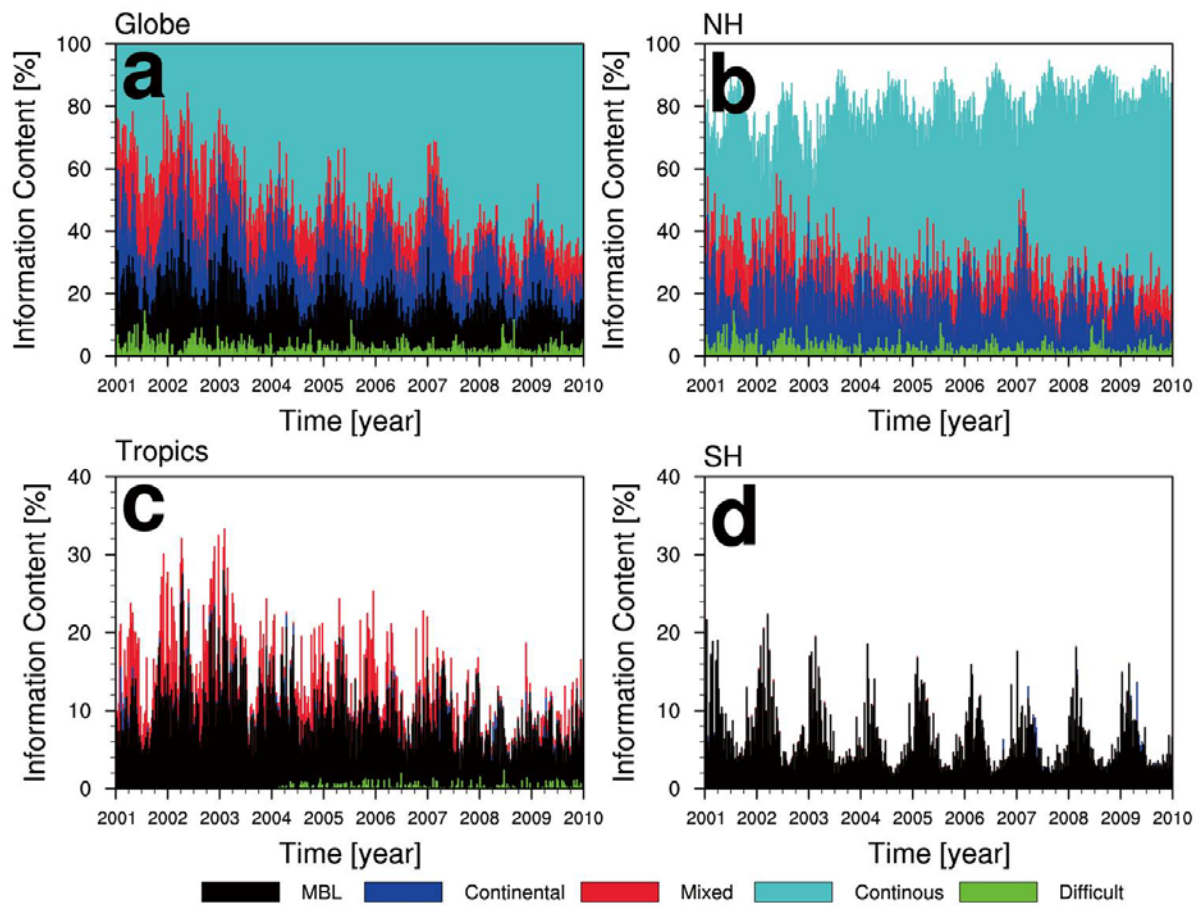
3 Figure 9. Average normalized information content for each observation site from 2000 to
 4 2009. The overlapping observation sites at the same locations or at close locations are
 5 distinguished using different sizes of circles.

6



1
2
3
4
5
6
7

Figure 10. Histograms of the average information content for each observation site category (a) around the globe and in the (b) Northern Hemisphere, (c) Tropics, and (d) Southern Hemisphere from 2000 to 2009. N(obs) in the upper right corner represents the number of observations used in data assimilation.

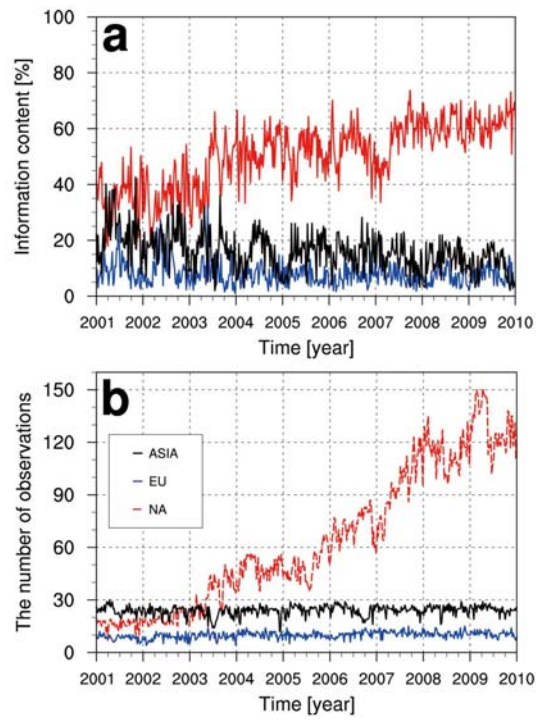


1

2

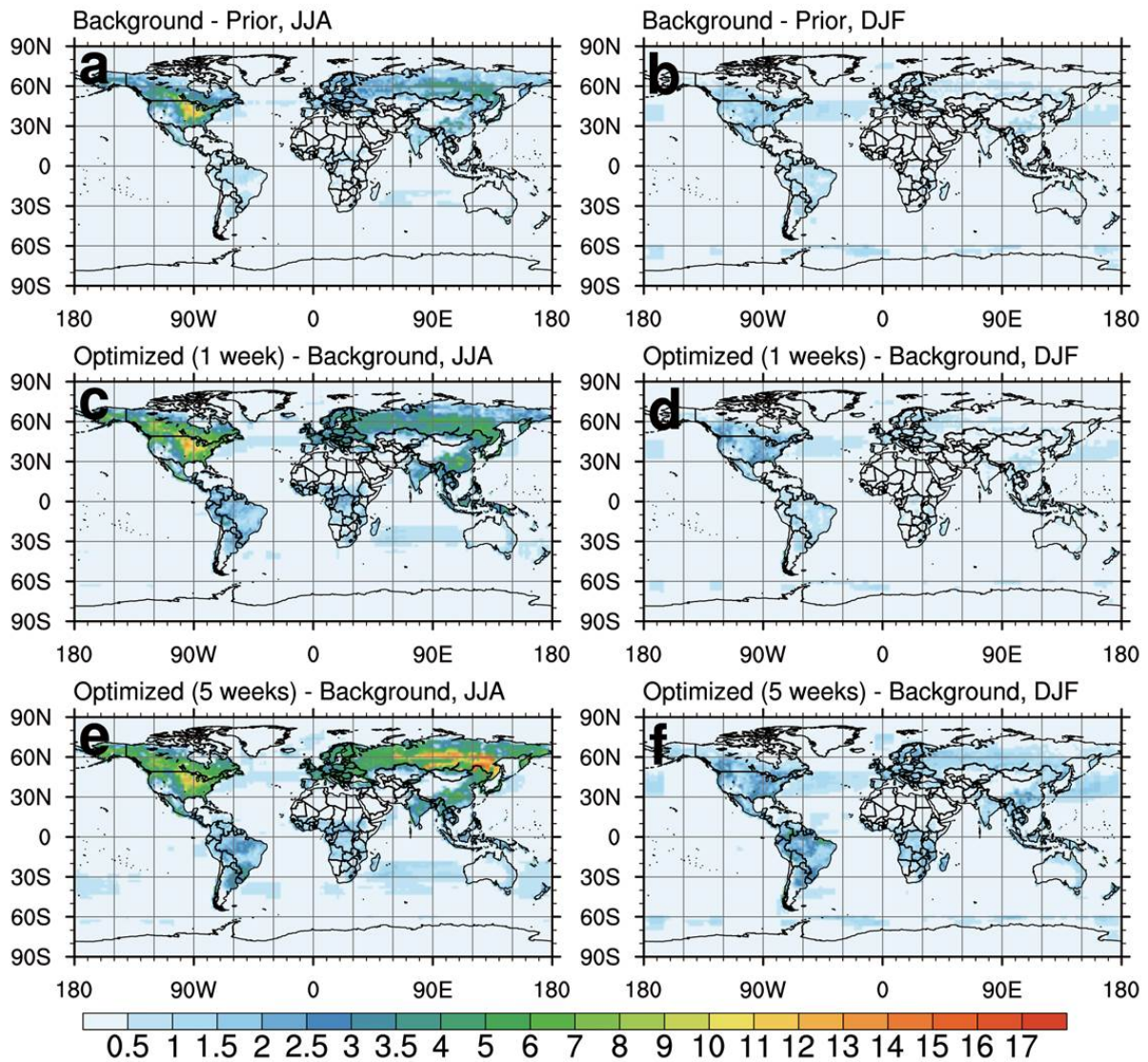
3 Figure 11. Time series of the average information content for each observation site category
 4 (a) around the globe and in the (b) Northern Hemisphere, (c) Tropics, and (d) Southern
 5 Hemisphere from 2000 to 2009.

6



1
2
3
4
5
6

Figure 12. Times series of the (a) weekly averaged information content and (b) number of observations in Asia (black line), Europe (blue line), and North America (red line) from 2000 to 2009.



1

2

3 Figure 13. Root mean square difference (RMSD) between the background flux and prior flux
 4 in (a) JJA and (b) DJF; RMSD between the background flux and posterior flux optimized by
 5 one-week observations in (c) JJA and (d) DJF; and RMSD between the background flux and
 6 posterior flux optimized by five weeks of observations in (e) JJA and (f) DJF. The units are g
 7 $\text{C m}^{-2} \text{ week}^{-1}$.